PKIKP Phase Back-Projection and Its Application on Southern Hemisphere Earthquake Imaging

Liuwei Xu[1], Lingsen Meng[1,*], Risheng Chu[2]

[1]Department of Earth, Planetary and Space Sciences, University of California Los Angeles, Los Angeles, CA, USA.

[2]State Key Laboratory of Geodesy and Earth's Dynamics, Innovation Academy for Precision Measurement Science and Technology, Chinese Academy of Sciences, Wuhan, China.

*Correspondence to: L. Meng, lsmeng@g.ucla.edu

Key Points

1. We identify optimal distance range for PKIKP phase in back-projection and get high-resolution images for earthquake sources.
2. PKIKP back-projection's resolutions and uncertainties are systematically evaluated, and are further validated by synthetic tests.
3. PKIKP back-projection is useful for imaging the source process of southern hemisphere earthquakes.

Abstract

Standard Back-Projections (BPs) use P phase recordings at large aperture arrays within teleseismic distances (30°-90°) to image earthquake sources. However, the majority of sizable arrays are in the northern hemisphere, leaving many southern hemisphere earthquakes beyond the teleseismic range. This paper studies the effectiveness of the PKIKP phase traveling through the Earth's core in the BP method. We identify the optimal distance range for the PKIKP BP as 150°-180°. We evaluate its resolution using array response functions and theoretical seismograms and test uncertainties by adding noise to coherent waveforms. Tests show that, within the optimal distance range, PKIKP BP achieves resolutions and uncertainties comparable to P phase BP. We validate the method using synthetic models of point sources and unilateral ruptures and demonstrate accurate recovery of rupture location, length, and speed. Applying PKIKP BP to the 2010 Mw8.8 Chile, 2021 Mw7.2 Haiti, and 2021 Mw7.4 and Mw8.1 Kermadec earthquakes, we compare our results with published BPs and/or slip models, confirming the feasibility and reliability of the method. We also find that waveform and wavefront distortions of the PKIKP phase within an array are minor and comparable to those of the P phase, further supporting the robustness of the method. These results suggest that PKIKP BP can serve as a powerful tool for source imaging and hazard assessment in regions such as the southwest Pacific, the western coast of South America, the South Sandwich Islands, and the southern Indian Ocean, where P-phase BP is limited or unavailable.

Plain Language Summary

Back-projection (BP) is an earthquake source imaging method that uses P-phase recordings at teleseismic distances (30°–90°) to track rupture propagation. This study advances the BP technique by incorporating the PKIKP phase—waves that travel through the Earth's core—to extend its capability for global earthquake imaging. The method is validated through resolution tests, uncertainty analyses, and synthetic simulations, showcasing its theoretical applicability. Application of the PKIKP BP method to well-studied earthquakes yields results that align with published studies, validating its reliability in depicting rupture processes. This advancement provides a promising avenue for investigating large earthquakes in the Southern Hemisphere, especially in regions such as the southwest Pacific, the western coast of South America, the South Sandwich Islands, and the southern Indian Ocean, where conventional BP using direct P waves is limited or unavailable. By providing better imaging in these under-monitored areas, the method will help improve our understanding of how major earthquakes rupture and the hazards they pose worldwide.

Index term

Earthquake source observations (1240)

Keywords

Back projection; PKIKP phase; southern hemisphere earthquakes

1. Introduction

Characterizing the kinematic history of large earthquake ruptures is a crucial aspect of seismological studies. Following a significant event, seismologists strive to promptly estimate rupture parameters, including slip distribution, rupture speed, and stress drop, in order to better assess potential hazards. Back-Projection (BP), a popular source-imaging technique, utilizes coherent seismic wavefields recorded by dense networks to track the growth of earthquake ruptures (Ishii et al., 2005; Kiser & Ishii, 2017). To obtain high-quality and high-resolution BP images of earthquake sources, large-aperture arrays with dense seismic stations at teleseismic distances (30°-90°) are required (Kiser & Ishii, 2017). These arrays have been installed on major continents such as North America, Europe, Australia, and Alaska, and have successfully been applied to image large earthquakes worldwide (e.g., Bao et al., 2019; Kehoe et al., 2019; Calais et al., 2022; Bao et al., 2022).

In standard BP techniques, the direct P phase recorded at teleseismic distances ($30° < \Delta < 90°$) is commonly employed due to its high coherence and minimal interference from other phases. However, for earthquakes occurring in certain regions of the southern hemisphere (e.g., New Zealand, Indian Ocean, Sandwich Islands), the availability of direct P phase is limited. This is primarily due to the fact that most large-aperture arrays on the northern continents are situated at distances exceeding 90°. In the case of southern hemisphere arrays, parts of the Australian array may fall within a range closer than the desired 30°. Seismic data in Africa and Southeast Asian islands arrays are not continuously available, further exacerbating the scarcity of useful stations for earthquake imaging. Moreover, the linear arrangement of stations along the west coast of South America presents challenges in achieving sufficient distance or azimuth coverage for BPs. While previous studies have utilized alternative seismic phases either to improve lateral- and depth-resolution (pP, Chen et al., 2018; PKP and PKIKP, Kiser & Ishii, 2012) or to provide comparisons for P phase BPs (e.g., PKIKP, PKP, PP; Koper et al., 2012), these phases have not been systematically evaluated in terms of their resolutions, uncertainties, and viable distance ranges.

In this study, we apply MUltiple SIgnal Classification (MUSIC) BP (Meng et al., 2011) to PKIKP waves, which travel through Earth's inner and outer cores, to track rupture propagation during large earthquakes. To solidly establish our method, we first analyze the resolution and uncertainty of PKIKP BP by calculating array response functions, back-projecting theoretical seismograms, and conducting noise bootstrap tests. To evaluate potential contamination from the trailing PKPab and PKPbc phases, we apply PKIKP BP to two magnitude 5–6 earthquakes and confirm the absence of artificial sources in the resulting BP images. Additionally, we perform BP using theoretical synthetic seismograms that include both PKIKP and PKP phases, demonstrating that the influence of PKP phases on PKIKP BP imaging is minimal. We further validate our approach by constructing seismograms using realistic empirical Green's functions, where the BP results accurately recover the spatiotemporal characteristics of the input rupture models. To assess the applicability of PKIKP BP to natural earthquakes, we examine the waveform coherence of the PKIKP phase across large-aperture arrays and apply our method to the 2010 Mw 8.8 Chile earthquake, the 2021 Mw 7.2 Haiti earthquake, and the 2021 Mw 7.4 and Mw 8.1 Kermadec earthquake doublet. The resulting BP images are consistent with published BP and/or finite-fault models. Finally, we assess the waveform and wavefront distortion of PKIKP phase, and discuss the advantages, limitations, and potential improvements of the method. Our findings demonstrate that in seismically active regions of the southern hemisphere, PKIKP BP can independently image earthquake sources, reliably resolve rupture characteristics, or serve as a reference for teleseismic BP results. The application of PKIKP BP thus broadens the range of usable arrays for earthquake source studies, offering valuable insights and enhancing our understanding on rupture processes of large seismic events.

2. Method and Data Processing

2.1 PKIKP BP

BP is a technique used to track the process of earthquake ruptures by capturing the spatial-temporal evolution of high-frequency (HF) radiators during mainshocks. These HF radiators are considered indicative of the rupture front (Yin & Denolle, 2019) and provide information about rupture kinematic characteristics such as directivity, source dimension, and rupture speed. The conventional BP analysis primarily relies on P phases recorded at teleseismic distances. In our PKIKP BP, we employ the same algorithm as the standard MUSIC BP (Meng et al., 2011) but utilize PKIKP phase recordings obtained at near-antipodal distances (150°–180°) from the Incorporated Research Institutions for Seismology (IRIS), Observatories & Research Facilities for European Seismology (ORFEUS), and China National Seismic Network. We download the vertical component of broadband seismograms (BHZ), which are then normalized by the initial PKIKP arrivals. To ensure accurate alignment, all waveforms are first automatically aligned based on the travel times predicted by a 1-D reference Earth model. Any remaining time errors between the predicted and actual arrivals are calculated and corrected by cross-correlating the first PKIKP phase arrival (Ishii et al., 2005). This time correction process involves four manual alignments. In each alignment, a reference station is chosen, and cross-correlation coefficients (CCs) of the filtered waveforms within a specific time window centered at phase arrivals between the reference station and all other stations are computed. Waveforms could be shifted slightly to achieve the highest CCs, and stations with CCs below a specified threshold are removed. The parameters for the first three alignments are as follows: [0.1-0.25 Hz frequency band, 20 s time window, 0.6 threshold], [0.25-0.5 Hz frequency band, 10 s time window, 0.6 threshold], and [0.5-1 Hz frequency band, 8 s time window, 0.6 threshold]. The final alignment also uses [0.5-1 Hz frequency band, 8 s time window, 0.6 threshold], but the reference waveform is the average waveform of all stations retained after the third alignment.

In BPs, the PKIKP waves are filtered to 0.25-1 or 0.5-1 Hz which ensures high resolution and keeps enough signal-to-noise-ratio (SNR). The subsequent rupture front is then imaged using the differential travel time relative to the mainshock hypocenter. It is important to note that as the rupture expands, the apparent rupture time may deviate from the actual rupture time: if the rupture moves towards the array, the actual rupture time should be later than the apparent one, whereas if the rupture moves away from the array, the actual rupture time is earlier than the apparent one (Figure S1 in Supporting Information S1). To correct for this effect, we deduct the mean travel time difference between the moving source and the hypocenter from the rupture time (Yao et al., 2011; Du, 2021). Finally, the MUSIC BP algorithm is applied to the aligned and corrected waveforms in 10-s-long sliding windows with an increment of 1 s to identify the HF radiators (for more details about the MUSIC BP, refer to Meng et al., 2011).

2.2 Resolution Analysis by Array Response Functions and Theoretical Seismograms

The array response function (ARF, Rost & Thomas, 2002) characterizes the imaging result of BP for a pulse-like point source located at the hypocenter. It provides information about the spread or leakage of beam power in the spatial domain:

$$|A(\mathbf{k}-\mathbf{k_0})|^2 = |\frac{1}{N}\sum_{n=1}^{N} e^{2\pi i(\mathbf{k}-\mathbf{k_0})\cdot\mathbf{r_n}}|^2 \tag{1}$$

where n is the station index, $\mathbf{r_n}$ is the location vector of the nth station, $\mathbf{k}$ is the wave number vector of any grid in the source region and $\mathbf{k_0}$ is the wave number vector of the hypocenter, N is the total number of stations.

In some numerical calculations, the vector product of the wave number $\mathbf{k}$ and the location vector $\mathbf{r_n}$ can be expressed in terms of travel time as $(\mathbf{k} - \mathbf{k_0})\cdot\ \mathbf{r_n} = f\,(T - T_0)_n = f\,(T_n - T_{0,n})$, where f is the frequency, $T_{0,n}$ is the travel time from the hypocenter to the n-th station, and T_n is the travel time from a given grid point in the source region to the n-th station. The equation (1) then becomes:

$$|A(\mathbf{k}-\mathbf{k_0})|^2 = |\frac{1}{N}\sum_{n=1}^{N} e^{2\pi i f(T-T_0)_n}|^2 \tag{2}$$

ARFs typically exhibit elliptical or circular shapes, which depend on the array's size and shape (Figures S2-S3 in Supporting Information S1). According to the Rayleigh criteria (Born & Wolf, 1999), the full width at half maximum (FWHM, the distance between the points on the curve at which the function reaches half of its maximum value) of the ARF represents the minimum distance required to distinguish between two closely spaced sources. Therefore, a smaller FWHM indicates a better resolution. To quantitatively assess the resolution of PKIKP BP, we calculate the ARFs for the P and PKIKP phases. We measure the FWHMs in two directions: the radial direction, which is parallel to the great circle path connecting the epicenter and the array center, and the tangential direction, which is perpendicular to the radial direction. For simplicity, we first consider a 1D linear array to establish the relationship between resolution and the ray parameter. In Supplementary Text S1, we conduct analytical analysis and discover that the resolution of the 1D array is positively correlated with the spatial derivative of the ray parameters ($|\Delta p/\Delta d|$; Text S1 in Supporting Information S1, Figures 1b-c and S4 in Supporting

Information S1). Subsequently, we numerically compute the FWHM of the ARF for the 1D array configuration. The linear array consists of 91 stations with a spacing of 22 km (Figure 1a). It extends in an east-west direction, with the earthquake source located to the east of the array (Figure 1). We calculate the ARFs for the P phase within the 30°-90° range, and PKIKP phase within the 135°-180° range. Since the 1D array configuration lacks resolution in the tangential direction (Kiser & Ishii, 2012), we solely measure the radial resolution. The numerical results (Figure 1b) are consistent with the analytical analysis. In the case of the 1D array, the P phase BP achieves its best resolution at 90°, whereas the PKIKP phase BP yields optimal resolutions at 180°.

To better assess the resolution of PKIKP BP under a 2D array configuration, we compute theoretical seismograms for the PKIKP and P phases generated by a point source using the Direct Solution Method (DSM) software (Kawai et al., 2006; Takeuchi et al., 1996) (Figures 2a and 2c). A circular array with a diameter of 20° (approximately 2200 km; Figure 1d) is configured to resemble the aperture of a typical large array (e.g., the Australian array). We then perform BP of both P and PKIKP phases using these synthetic seismograms filtered to 0.25-1 Hz. The resulting BP image is treated as a resolution kernel (Figures 2b and 2d), from which we measure the FWHM. As in the 1D analysis described above, a smaller FWHM indicates higher resolution. The FWHMs in the radial and tangential directions are shown in Figure 1e. For the PKIKP phase, the median FWHMs within the 150°–180° epicentral distance range are approximately 31 km in the radial direction and 25 km in the tangential direction. For comparison, the P phase BP within the 30°–90° distance range yields median FWHMs of about 22 km (radial) and 8 km (tangential). While the resolution of PKIKP BP is somewhat lower than that of P phase BP, it remains comparable, supporting the suitability of PKIKP BP for earthquake source imaging.

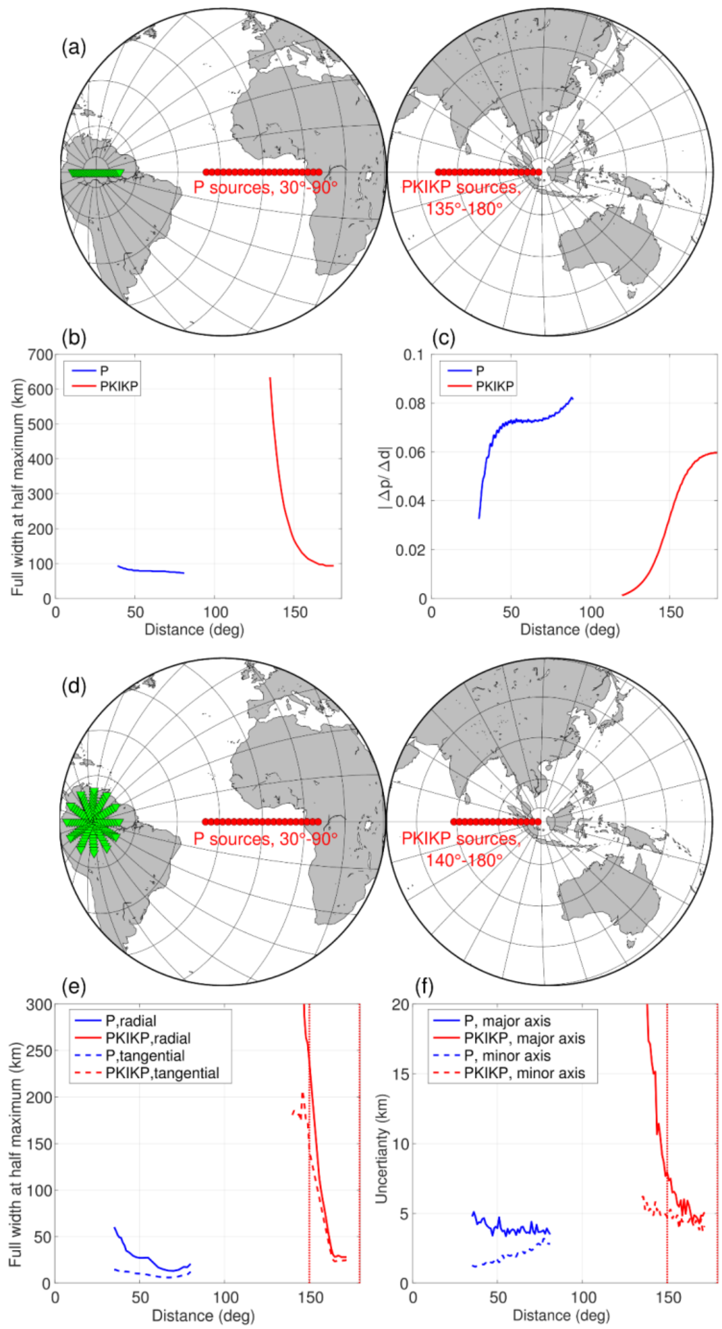

Figure 1. The resolution analysis and uncertainty test results. (a) The linear 1-D array configuration and source distribution. Green triangles denote the stations. Red circles denote P and PKIKP sources tested in ARF analysis. (b) The full width at half maximum (FWHM) of the 1-D arrays' ARFs for P and PKIKP BPs at different distance ranges. (c) The spatial derivative of ray parameter v.s. distance. *p*: ray parameter; *d*: epicenter distance. (d) The circular 2-D array configuration and source distribution. (e) The FWHM of the 2-D arrays' resolution kernel for P

and PKIKP BPs at different distance ranges. The solid lines denote the FWHM in radial distance. The dash lines denote the FWHM in tangential direction. The red dotted lines encompass the useful range of PKIKP phase BP. (f) The major (solid lines) and minor (dash lines) axis lengths of the 95% confidence bound of the perturbed BP locations.

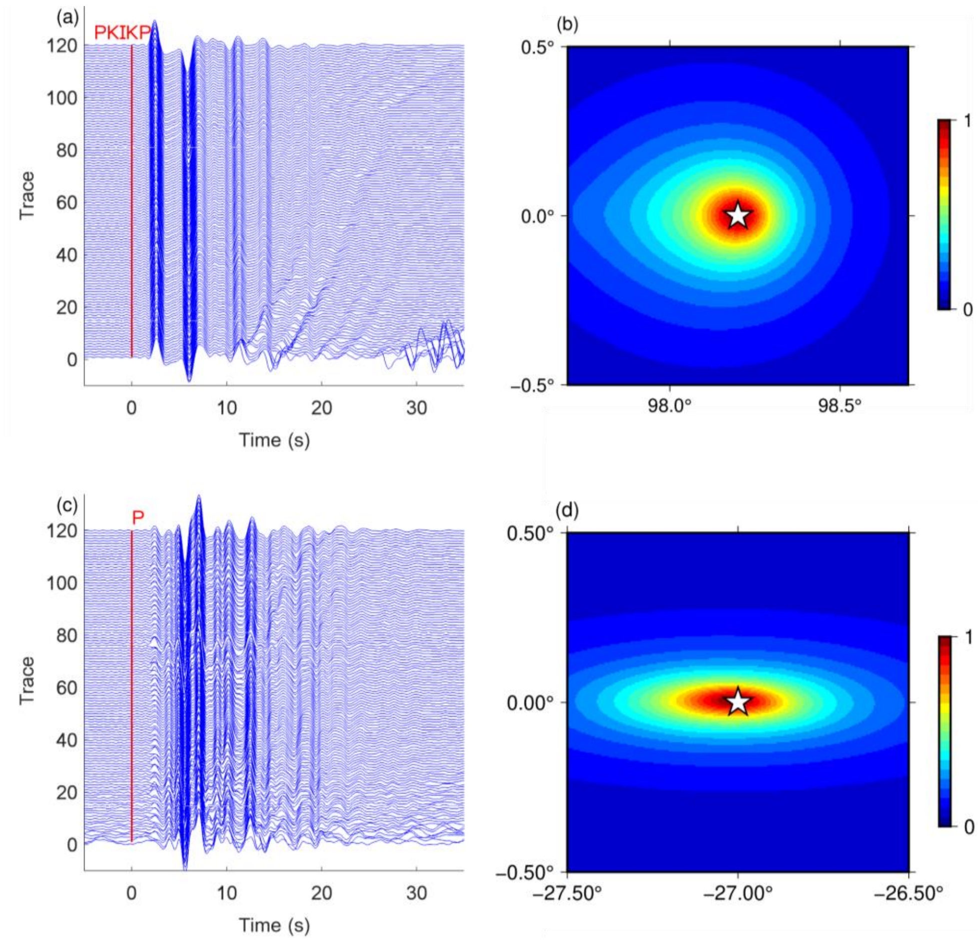

Figure 2. Examples of theoretical waveforms and resolution kernels. (a) PKIKP phase waveforms at an epicentral distance of 165°. The red line indicates the predicted arrival of the PKIKP phase. (b) Resolution kernel for PKIKP BP. The white star marks the epicenter. (c) P phase waveforms at an epicentral distance of 40°. (d) Resolution kernel for P phase BP.

2.3 Robustness Analysis by Theoretical Seismograms

To assess the uncertainties of PKIKP BP resulting from noise, we conduct bootstrap tests. We adopt the same 2D array configuration as in Section 2.2 and use the corresponding theoretical seismograms, extracting 10-second waveforms centered on the first arrivals of each phase to serve as coherence signals. In order to simulate the effects of ambient noise, we introduce white noise to the coherence signals. We shift the waveforms based on the travel time predicted by the 1D Earth model. The amplitudes of the coherent signals and the noise are normalized to achieve a signal-to-noise ratio (SNR, std[signal]/std[noise]) of 5 in the frequency range of 0.25 to 1 Hz. One hundred synthetic realizations of coherence seismograms plus white noise are then back-projected to obtain the perturbed BP locations. The 95% confidence bounds of the perturbed BP locations generally exhibit elliptical shapes, and we measure the lengths of the major and minor axes of these ellipses (Figures 1f, S5-S6 in Supporting Information S1). For P phase BP, the median lengths of the major and minor axes are approximately 3.8 km and 2.2 km, respectively. For PKIKP BP at hypocenter distances of 150°-180°, the median lengths of the major and minor axes are around 4.9 km and 4.4 km, respectively. We repeat the procedure for different noise levels (SNR = 3, 4, 6) observed in different magnitude earthquakes, and all the results are presented in Figure S7 in Supporting Information S1. The small locating errors caused by noise indicate that at near antipodal distances (>150°), the noise-induced uncertainties of PKIKP BP are sufficiently small.

2.4 Potential Influence From Other Core Phases

2.4.1 ARF of Propagating Ruptures Involving Multiple Core Phases

Core phases travel through multiple layers inside the Earth, following complex paths that result in multiple phase arrivals (Tkalčić et al., 2002, Garcia et al., 2004). At distances ≥150°, PKIKP is the first arrival, followed by PKPab and PKPbc phases. At 150°, the separation time between PKIKP and PKPab is approximately 14 seconds (Garcia et al., 2004), and this separation increases with greater epicentral distances. For a shallow earthquake (10 km depth), the separation times are roughly 40 s at 160°, 75 s at 170°, and 95 s at 175° (Kennett, 1991). We therefore compute the ARF for a dynamic rupture scenario to evaluate the impact of the PKPab and PKPbc phases on PKIKP BPs (Text S2 in Supporting Information S1). In this scenario, the rupture initiates at the epicenter (denoted by the red star in Figure S8 of Supporting Information S1), spans 200 km, propagates northward at a speed of 2 km/s, and lasts for 100 seconds. In the calculation, the PKIKP phase is treated as the signal, while the subsequent PKPab and PKPbc phases are considered as potential disturbance. Specifically, the travel time used to compute the ARF corresponds to the PKIKP phase, while the waveforms are a mixture of PKIKP, PKPab, and PKPbc phases (Equation 12 in Supporting Information S1). Our results demonstrate that, throughout the rupture process, only the BP power corresponding to the PKIKP phase is observed. Although the PKP phases begin to arrive after 6 seconds, it only introduces minor aliasing in the BP power and does not generate artificial sources or substantially affect the PKIKP source locations (Movies S1 and S2).

2.4.2 PKIKP BP on M5-6 events

We then apply our method to two events with magnitudes of 5.8 and 5.3 (EGFs 1-2 in Table S1 of Supporting Information S1) to assess the influence of later phases (e.g., PKPab, PKPbc) on the PKIKP BP of natural earthquakes. These magnitude 5-6 events can be considered as simple point sources in BP studies. The start time of the BP is set to coincide with the PKIKP arrival time, and the BP duration is set to 100 s, which is much longer than the typical duration of magnitude 5-6 events. This extended duration is intended to capture any potential influence from later phases, should they have any effect. Additionally, we set the spatial range for the BP as follows: longitude from [hypocenter_lon - 3] to [hypocenter_lon + 3], and latitude from [hypocenter_lat - 3] to [hypocenter_lat + 3]. This spatial range is significantly larger than the rupture extent of magnitude 5-6 events and is also intended to detect any possible influence from later phases. In BP analysis, we typically require the detected energy pulses appearing in both spatial and temporal domains to be concentrated to interpret BP images as true sources. This requires not only a high BP power level but also the sources should appear stable (e.g., duration >3 s, Feng et al., 2020) and well-defined (e.g., the peak stands out due to its intrinsic height and its location relative to other peaks, Feng et al., 2020) in the BP movies/snapshots. The core-phase waveforms of EGF1 are plotted in Figure S9, where the move-out of the PKPab phase is visible following the PKIKP phase. We also plot the BP power evolution over the 100-second window. As shown in Figure S10c in Supporting Information S1, only one BP power peak appears in the evolution curve, occurring around 10 s. The corresponding HF radiators are concentrated at their respective epicenters (Figures S10a-b in Supporting Information S1, Movies S3-S4). After 15 s, the power drops to a very low level, and the radiators become scattered and unstable (Figures S10a-b in Supporting Information S1, Movies S3-S4). The low power level and unstable radiators result from the dominance of coda waves in the waveforms, which means they would not be considered part of the BP results. Here, the BP power pulse length (~15 s) is longer than the typical source duration of magnitude 5–6 events (~1 s; Gomberg et al., 2016) because both the source slip-rate function and the Green's function have finite durations that contribute to the overall pulse length. These two cases demonstrate that, for a simple point source, PKIKP BP can accurately image the source location, and later phases do not result in apparent multiple events in the BP image.

2.4.3 BP on Theoretical Seismograms Involving Multiple Core Phases

We further evaluate the potential influence of PKP phases on the BP image of large earthquakes by performing PKIKP BP on theoretical seismograms. The seismograms are computed using the DSM software for three scenarios: (1) a point moment tensor source, (2) a westward-propagating rupture, and (3) a northward-propagating rupture. The point source has the same focal mechanism as the 2010 Mw 8.8 Chile earthquake but a moment magnitude of 6.1. The receiver station configuration is the same as that used in Sections 2.2 and 2.3 (Figures 1d & S11c). Stations are distributed within a 152°–172° epicentral distance range. In the point-source scenario, all PKIKP, PKPbc, and PKPab phases appear in the seismograms (Figure S11a). For the west-propagating rupture, we model a 100 km rupture length with a rupture speed of 1 km/s by stacking seismograms from ten evenly spaced sources along the rupture path, accounting for epicentral distance changes and time delays. The synthetic seismograms exhibit waveform complexity due to PKP phases following PKIKP (Figure S11b). However, the synthetic PKIKP BP successfully recovers the input rupture path, length, and speed (Figure S11c-d), demonstrating minimal influence from these disturbing phases. Similarly, the BP results for the northward-propagating rupture scenario also accurately reconstruct the input rupture length, orientation, and speed (Figure S12), further supporting the robustness of our method.

3. Validations With Synthetic Tests

3.1 Synthetic BPs on Dynamic Rupture Scenarios

In real earthquakes, waveforms often exhibit complexities such as scattering and coda waves, making them more intricate than theoretical seismograms. To simulate these realistic features and evaluate the performance of our method under more practical conditions, we perform PKIKP BP on synthetic waveforms generated by summing the slip-rate contributions from each subfault and convolving them with empirical Green's functions (EGFs). The EGF used for the P-wave synthetic test is a magnitude 5.8 event that occurred in central China and was recorded by the Europe array (EGF 3 in Table S1 in Supporting Information S1). For the PKIKP synthetic BP, the EGF is a magnitude 6.1 event that occurred north of New Zealand and was recorded by the Europe array (EGF 4 in Table S1). All waveforms begin at the P/PKIKP arrivals and extend to 120 seconds thereafter. The input source model has a 5-m uniform slip and unilateral rupture on the vertical fault. The fault surface dimensions are 100-km-long and 10-km-wide, and the moment magnitude is Mw 7.45 assuming a 30 GPa rigidity. The slip model is discretized into elements with a size of 10 km × 10 km, and the rupture propagation speed is set at 2 km/s. The slip-rate function used in the simulations is the Yoffe analytical function (Yoffe, 1951; Tinti et al, 2005). Two sets of tests are configured: one with the rupture propagation direction perpendicular to the great circle paths connecting the seismic sources and the center of the array (orthogonal-path test; Figure 3 and Figures S13-S14 in Supporting Information S1), and the other one with rupture propagating along the great circle path (along-path test; Figures S15 in Supporting Information S1). In each set, two phases are tested: direct P phase in the range of 50°-80°, and PKIKP phase in the range of 150°-180°. The epicenters for the synthetic tests are located at (28.40°N, 104.93°E) for the P phase, and (34.59°S, 178.41°W) for the PKIKP phase. The synthetic BP time durations are 50 seconds for all tests, based on the rupture length and speed.

In Figure 3, the results of the orthogonal-path test are presented. It can be observed that the spatiotemporal locations of the propagating rupture fronts recovered by the P and PKIKP phase BPs are generally consistent with the input model. The resolved rupture lengths and speeds are also very close to the model settings. For the PKIKP phase BP, the imaged HF radiators occasionally deviate from the input rupture front in the tangential direction (Figure 3d). However, the along-strike rupture length is well recovered (Figure 3e). The results of along-path test are presented in Figure S15. Before 40 s, the rupture process is well recovered by PKIKP BP. After 40 s, the tailing artifacts, which are often observed at the end of the rupture process and can be attributed to the relatively weak coherent signals and strong coda waves in the late stages (Bao et al., 2022), contaminate the imaged rupture front, and make the rupture length underestimated by ~25%. We note that the synthetic BPs' performance on the along-path test is worse than that on the orthogonal-path test, which is consistent with resolution and uncertainty analysis in Section 2. It suggests that caution should be taken when interpreting similar rupture scenarios in natural earthquakes. Despite these artifacts, the overall performance of the PKIKP BP in tracking the rupture evolution remains reliable.

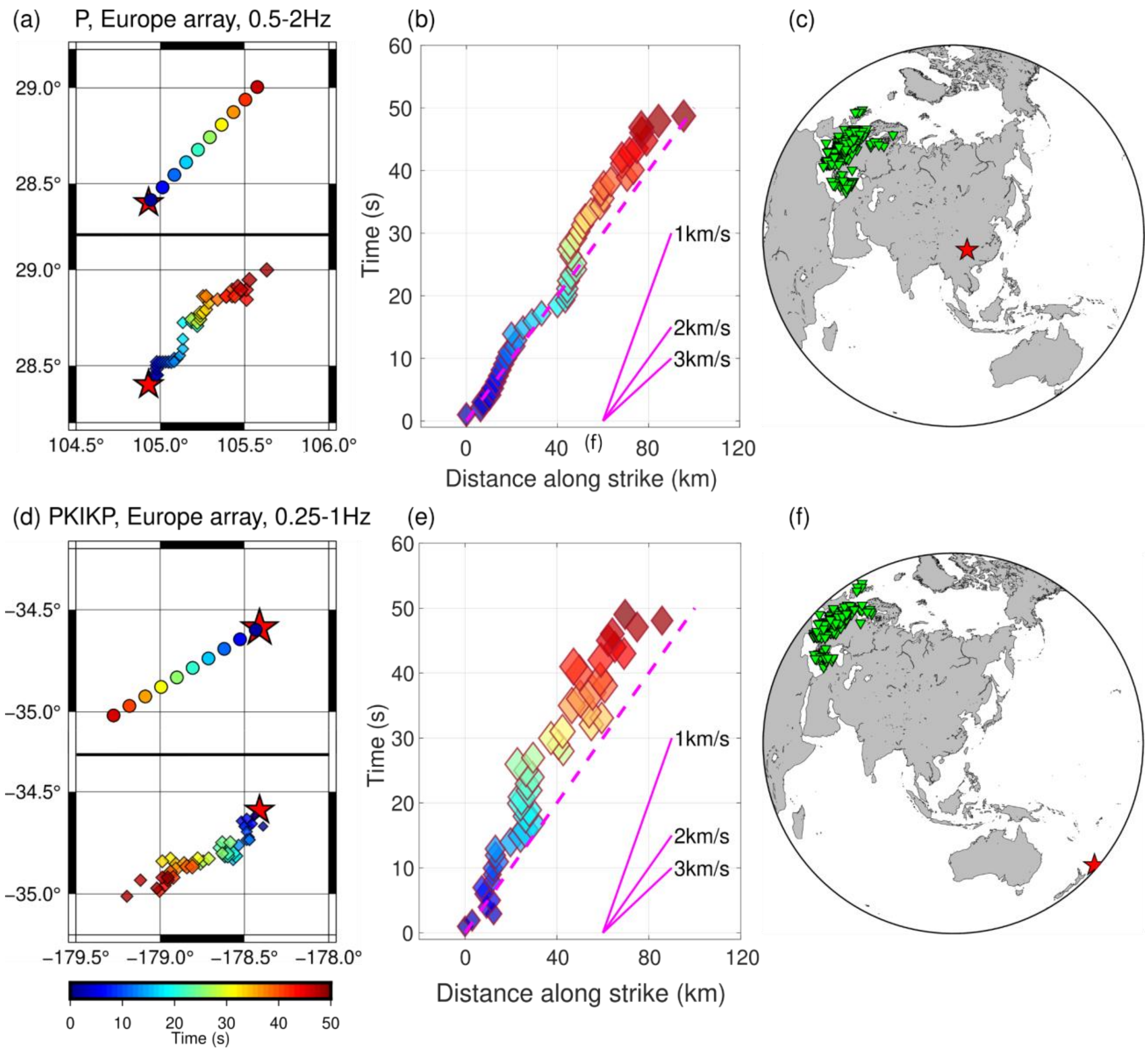

Figure 3. Synthetic BP results (orthogonal-path test). (a) Synthetic BP of P phase at 50°-80°. Solid circles are the input rupture, and semi-transparent diamonds are imaged HF radiators color-coded by rupture time. (b) The along-strike distance of HF radiators imaged by P phase BP. The magenta dashed line indicates the input rupture speed (2 km/s). (c) The stations used for P phase BP. Green triangles denote the stations and the red star denotes the epicenter. (d) The same as (a)

but for the PKIKP phase at 150°-180°. (e) The same as (b) but for the PKIKP phase. (f) The same as (c) but for the PKIKP phase.

3.2 BP Uncertainty Due to Incoherent Noise

The synthetic waveforms built based on EGFs allow us to estimate the uncertainty caused by realistic noises (e.g. coda waves, local scattering). To achieve this, we employ a bootstrapping approach. First, the peak in the orthogonal-path test BP images serves as the reference point-source location for each time step. Within each time window, we shift, stack, and average the array waveforms based on the time shift predicted by this reference location. The resulting mean seismograms are taken as a representative of the coherent signal. To assess the incoherent noise at each station, we calculate the waveform residual concerning the mean seismogram. This residual is treated as incoherent noise. We randomize the Fourier phase spectrum of the incoherent noise and stack it back to the mean seismogram. This procedure models the random phases of scattering waves while preserving the amplitude spectrum of the waveform. One hundred synthetic realizations of the mean seismogram, each combined with incoherent noise, are subsequently subjected to BP to determine the perturbed BP source locations for each time step. Figures S16a-S16b in Supporting Information S1 present ellipses delineating the 95% confidence bounds on the BP radiator locations. The median lengths of the major and minor axes are 9.6 by 3.5 km and 14.8 by 9.4 km for P and PKIKP BPs, respectively. The analysis indicates reasonably small uncertainties generated by noise for the PKIKP BP. These synthetic tests demonstrate the capability of PKIKP BP to accurately track the spatial-temporal evolution of rupture fronts.

4. PKIKP BP Applications

To validate the performance of PKIKP BP in imaging natural earthquakes, we apply it to four earthquakes, and compare the results with published P phase BPs and/or finite fault slip models. The first event is the 2010 Mw 8.8 Chile earthquake, which occurred on February 27 at Chile's Maule region. The second earthquake is the Mw 7.2 one that struck Haiti on August 14, 2021, with a clear surface rupture trace. The third and fourth events are an earthquake doublet that occurred in the Kermadec Islands near New Zealand on March 4, 2021, consisting of a Mw 7.4 foreshock followed by a Mw 8.1 mainshock. For the 2010 earthquake, we utilize the PKIKP phase recorded at the Asian array (Figures 4a, c and S17-S18). As a point of comparison, we also apply the P phase BP to recordings obtained at USArray (Figure 4b, d and Text S3 in Supporting Information S1). For the 2021 Haiti earthquake, we collect PKIKP waves from the Australia and Southeast Asia array (Figures 5 and S19), and compare the results with P phase BP and surface fault traces identified from satellite observations (Calais et al., 2022; Yin et al., 2022). For the 2021 Kermadec earthquake doublet, we collect PKIKP recordings from the European array (Figures 6-7 and S20-S21), and P phase recordings from the Australian and Chinese arrays (Figures 6-7). We then compare and discuss the resulting BP images from three arrays.

4.1 The 2010 Mw 8.8 Chile Earthquake

4.1.1 Review of Previous Studies on The Rupture Kinematics

The Mw 8.8 Chile earthquake, one of the most powerful earthquakes in decades, caused significant damage and had a profound impact on the local population. The earthquake struck the coast of central Chile, near the Maule region. Many source observation studies have been carried out to understand the rupture process of this megathrust earthquake, including both BP and finite fault inversions (Delouis et al., 2010; Huang et al., 2017; Kiser & Ishii, 2011; Koper et al., 2012; Palo et al., 2014; Pollitz et al., 2011; Zhang, 2018). Overall, the earthquake exhibits an asymmetrical rupture pattern, with one branch propagating to the north-northeast and the other to the south-southwest (Lay et al., 2010; Tong et al., 2010; Vigny et al., 2011; Koper et al., 2012; Moreno et al., 2012; Lin et al., 2013). The rupture extends approximately 450 km along strike. The joint finite fault inversion conducted by Yue et al. (2014), which integrates teleseismic, local GPS, Interferometric Synthetic Aperture Radar (InSAR), and tsunami datasets, reveals that the northern branch extends ~240 km and the southern branch ~200 km. The peak slip (~16 m) occurs 120-200 km north of the hypocenter at a depth of 16 km (Figure 4a). To the south, the maximum slip reaches 12 m near the trench. This asymmetric slip distribution is consistent with results from Koper et al. (2012) and Pollitz et al. (2011), both of which show smaller coseismic slip south of the epicenter compared to the north.

Previous BP studies show that HF radiators propagated northward over distances ranging from ~300 km (Zhang, 2018; Huang et al., 2017) to ~500 km (Palo et al., 2014), with rupture speeds of 2.5–3.0 km/s (Koper et al., 2012). These results primarily rely on data from the USArray, whose azimuth relative to the epicenter aligns with the strike of the northern branch (Figure 4b), allowing for a good resolution of the northern rupture. In contrast, the unfavorable azimuthal positioning of the southern branch, combined with its smaller coseismic slip, reduces the detectability of the southern rupture propagation in BP analyses. This limitation likely contributes to discrepancies in previous estimates of the rupture direction, length, and speed along the southern segment. For example, Zhang (2018) used teleseismic P-phase BP and estimated a southern rupture length of ~175 km with a rupture speed of 1.84 km/s. While the BP image from Palo et al. (2014) shows beam power south of the epicenter, it does not clearly resolve a southern HF radiator. High-frequency (1–5 Hz) BP results from Kiser and Ishii (2011) identify a southern segment near 37.5°S at ~70 s, with a rupture speed of ~0.8 km/s and a duration of ~25 s.

An interesting observation in previous studies is that the short-period radiations differ from the regions of large coseismic slip: most of the slip inverted by long-period and broadband data occurs offshore in shallower regions, while the short-period radiators originate from greater depths within the subduction zone (Lay et al., 2012). This depth-dependent pattern has been observed on subduction zones worldwide, such as in the 2011 Mw 9.0 Tohoku earthquake in Japan and the 2004 Mw 9.2 Sumatra earthquake, and may reflect along-depth variations in source properties such as rigidity or stress drop (Lay et al., 2012; Yao et al., 2011).

4.1.2 Waveform Coherence of PKIKP Phase

Waveform coherence plays a pivotal role in BP imaging. When dealing with P phase BPs, the initial arrivals, consisting of the first few wiggles of P-wave trains, exhibit a high degree of similarity among stations. This waveform similarity decays rapidly over time and over varying interstation distances due to interference from subsequent coda waves (Zhou et al., 2022). The coherence of these initial arrivals ensures that the corresponding source location can be accurately imaged by BP, while the presence of incoherent coda waves prevents earlier sub-sources from masking or interfering with subsequent ruptures (Bao et al., 2022). To assess the coherence of the PKIKP phase, the first 10 seconds of PKIKP waveforms recorded at the Asian array are chosen (Figure S22a in Supporting Information S1). Utilizing one station as the reference, CCs between all waveforms and the reference waveform are presented in Figures S22c in Supporting Information S1. For comparison, the same procedure is applied to P phase waveforms recorded at USArray for the same earthquake (Figures S22b, d in Supporting Information S1). Within the first 10 seconds of the PKIKP phase, waveforms recorded at most stations demonstrate high coherence with CCs ≥ 0.8, indicating the feasibility of its BP. As interstation distance increases, waveform coherence decreases, and this trend aligns with that observed for the P phase (Figures S22c, d in Supporting Information S1).

4.1.3 PKIKP BP Image of The 2010 Mw 8.8 Chile Earthquake

Our BP analysis indicates that the 2010 Chile earthquake exhibits bilateral rupture characteristics, extending in the north-northeast and south-southwest directions (Figure 4a, c). The south branch is well-resolved in the PKIKP phase BP, measuring about 150 km in length with a rupture speed of 2.6 km/s, while the north branch is approximately 300 km long with a rupture speed of 2.5 km/s (Figure 4c). The results from the teleseismic P BP consistently reveal a rupture process for the north branch, with an estimated length of approximately 300 km and a speed of around 2.5 km/s (Figures 4b, d). The PKIKP BP shows scattered BP radiators after 105 s, which are tailing artifacts (Bao et al., 2022) caused by weak coherent signals and dominant noises at the end stage of the rupture. Such tailing artifacts are also observed in teleseismic P BP of USArray (Figures 4b and 4d) but occur after 110 s. Furthermore, the PKIKP BP successfully resolves a clear rupture propagating southward between 0-20 seconds and 40-60 seconds, being consistent with the coseismic slip model (e.g., Yue et al., 2014) and suggesting a potentially continuous rupture branch to the south of the epicenter. The south branch imaged by PKIKP BP provides more rupture information than that by the teleseismic P BP (see Figure 4): in the teleseismic P BP, it appears that the south radiators apparently stagnate at the epicenter before 40 s, and only a few radiators are resolved between 40-60 seconds. This comparison underscores the advantage of PKIKP BP in imaging bilateral ruptures (for more discussion, refer to Section 4.1.5: BP for The Bilateral Earthquake). It also indicates the necessity of PKIKP BP when only one array is available for teleseismic BP, as is often the case in earthquakes occurring in regions like Chile.

4.1.4 Comparison With Previous Studies

Regarding the northern branch, our PKIKP BP results align with short-period radiators resolved by previous research (Figure S23 in Supporting Information S1; Kiser & Ishii, 2011, Palo et al., 2014). Notably, the PKIKP BP reveals additional details about the southern rupture: BP power from the south is radiated around 0-20 s and 40-60 s, and is located at 0-50 km and 100-150 km from the epicenter (Figure 4c). These features were not captured in previous BP results (Figure S23 in Supporting Information S1).

PKIKP BP was first applied by Koper et al. (2012) to the 2010 Chile earthquake using F-net data from Japan. Their results supported a bilateral rupture pattern, with a coherent burst of BP energy approximately 100–200 km northeast of the epicenter. However, due to the relatively small aperture of the array and the resolution limitations inherent to beamforming-based BP methods, the spatial location of HF radiators resolved by their PKIKP BP was considerably less certain than that of the P phase BP (see Figures 2 and 5–6 in Koper et al., 2012). Kiser and Ishii (2012) also investigated PKIKP BP by computing synthetic BP images for a point source located at the epicenter of the 2007 Mw 8.4 Mentawai Islands earthquake using the TA network in the western U.S. However, the array's epicentral distance (122°–141°) lies within a region where the spatial derivative of the ray parameter ($|\Delta p/\Delta d|$) is small (Figure 1c), and is outside the effective range identified in our study (150°–180°). As a result, the resolution kernel was large (see Figure 1e in this study and Figure S1c in Kiser & Ishii, 2012), indicating poor spatial resolution. In the same study, they also performed synthetic BP using the PKPbc phase from Hi-net in Japan for the 2007 Mw 8.0 Pisco, Peru earthquake. Similarly, the narrow distance range of the array (146°–150°) resulted in a large resolution kernel (Figure 9c in Kiser & Ishii, 2012).

The scarcity of large-aperture, densely distributed seismic networks, the inherent resolution limitations of beamforming-based BP, and the lack of a clearly identified effective distance range may explain why PKIKP BP has not been widely adopted over the past decade. With advancements in instrumentation and direction-of-arrival estimation techniques, such as MUSIC-based BP (Meng et al., 2011; 2012a), PKIKP BP now can offer sharper rupture imaging and improved resolution. For instance, for events in Chile and Peru, the China National Seismic Network covers a broader distance range (150°–180°), which significantly enhances radial resolution. Moreover, our study is the first to systematically evaluate the performance of PKIKP

BP across the 135°–180° distance range (Figure 1) and to identify an effective region for its application, providing a valuable reference for future array selection and BP applications.

4.1.5 BP for The Bilateral Earthquake

An inherent drawback of the teleseismic BP when imaging bilateral ruptures is the array-dependent effect: the BP analysis tends to capture the rupture front propagating toward the receiver array since the shorter wavelength due to Doppler effects leads to stronger apparent high-frequency beam power (Li et al., 2022a; Xu et al., 2023). The array-dependent effect is especially noticeable in cases like the 2010 Chile earthquake, where the USArray is the sole useful teleseismic array, positioned to the north of the earthquake's hypocenter (e.g., Koper et al., 2012; Palo et al., 2014). Based on the analyses and comparisons presented in the previous sections, the PKIKP BP outperforms the teleseismic BP in imaging this bilateral event. The advantage of the PKIKP BP is that the array is positioned at the antipode and has a smaller incidence angle (less than 5°) compared to the P phase (with incidence angles reaching up to 28°), effectively mitigating spatial bias. The improved performance of the PKIKP BP for this earthquake can also be partially attributed to the position of the Asia array; its relative azimuth is orthogonal to the direction of rupture propagation, which reduces array-dependent effects in the BP results. To further confirm the benefits of using PKIKP BP in resolving bilateral earthquakes, a synthetic test is conducted. The input rupture model consists of a bilateral rupture extending in N20°E and S20°W directions, each with a length of 100 km and rupture speeds of 2 km/s (Figures S24a, d in Supporting Information S1). The epicenter is set to be the same as the 2010 Mw 8.8 Chile earthquake. The vertical fault's lower boundary depth is set at 10 km, and it is discretized into 10 km by 10 km subfaults with a uniform slip distribution of 5 m. The Yoffe analytic function with a 5 s rise time is used as the slip-rate function. Synthetic waveforms are calculated as the sum of slip-rate contributions from each subfault, convolved with EGFs. The PKIKP phase EGF is recorded at the antipodal Asia array, and P phase EGF is recorded at USArray to the north of epicenter. The results, as shown in Figures S24b-c in Supporting Information S1, demonstrate that the PKIKP BP effectively resolves the south rupture after approximately 22 seconds. The radiators' times and locations align well with the input model. In contrast, the teleseismic P BP only images some south radiators between 40-50 seconds, with their locations deviating from the input model (Figure S24e-f in Supporting Information S1).

This synthetic test illustrates that for some bilateral ruptures, the PKIKP BP could potentially provide more information about the distal branch than the teleseismic P BP.

4.1.6 Spatial Bias Test Based on Aftershock Locations

HF radiators of large earthquakes often exhibit systematic location bias as the rupture propagates farther from the hypocenter (Meng et al., 2016; Zeng et al., 2022). This bias, manifested as deviations of BP-inferred locations from their true positions, is primarily caused by travel time errors introduced by heterogeneities in the Earth's three-dimensional structure. We select eight M6 earthquakes in the Chile earthquake source region to evaluate the spatial bias in PKIKP BP (Figure S25a in Supporting Information S1). For reference, P phase BP is also applied to these eight earthquakes (Figure S25b in Supporting Information S1). We adopt the same time corrections as the mainshock, thus the mismatch between the BP-inferred aftershock locations and the catalog locations could be used to evaluate the spatial bias of BP in the source region. The results of PKIKP BP are shown in Figure S25a in Supporting Information S1, and that of P BP are shown in Figure S25b in Supporting Information S1. We find that to the south of the hypocenter, the PKIKP BP-inferred locations are systematically biased northward for ~13.0 km, while at the north, the BP images are biased southeastward for ~12.5 km. The BP-inferred locations by the P BP are systematically northwestward. The root-mean-square (RMS) of spatial errors of all eight events in PKIKP BP is 14.7 km (Table S2 in Supporting Information S1), slightly smaller than that in P BP (21.8 km; Table S3 in Supporting Information S1).

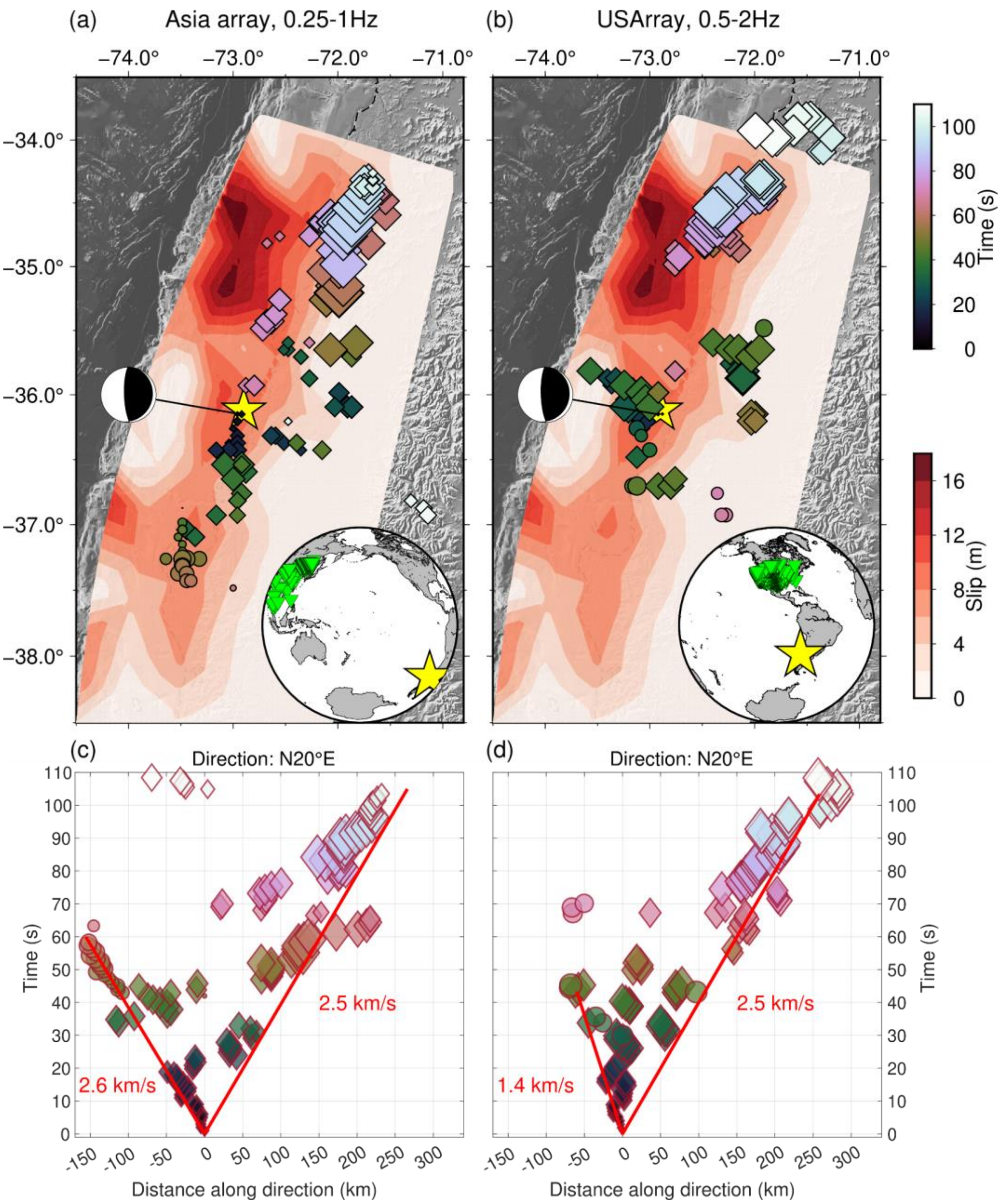

Figure 4. Comparison of BP results of the 2010 Mw8.8 Chile earthquake. (a) PKIKP phase BP results by the array in Asia. The diamonds are HF radiators color-coded by rupture time with their sizes proportional to the normalized BP power. The circles are HF radiators with secondary BP power peaks. The contours denote the slip model from Yue et al. (2014). The lower inset indicates the epicenter and the stations utilized. (b) P phase BP results by the USArray. (c) The along-direction distance of HF radiators in (a). Two lines and numbers show the linear regression of leading radiators (radiators with the largest epicentral distance at a given time) and rupture speeds. The circles are HF radiators with secondary BP power peaks. The positive direction is

N20°E, and the negative direction is S20°W. (d) The along-direction distance of HF radiators in (b).

4.2 The 2021 Mw 7.2 Haiti Earthquake

We select the 2021 Haiti earthquake as our second benchmark example to evaluate our method. The Mw 7.2 event struck the Southern Peninsula of Haiti on August 14 2021 (Figure 5a; Maurer et al., 2022; Okuwaki & Fan, 2022; Yin et al., 2022; Raimbault et al., 2023). Though the area is mostly rural, the earthquake resulted in ~2,500 dead, 13,000 injured, and at least 140,000 houses destroyed or damaged (Calais et al., 2022). This earthquake has a source mechanism combining strike-slip and reverse faulting and exhibits a clear surface rupture trace, as depicted in the ground deformation map obtained through InSAR imaging (Figure 5; Yin et al., 2022). The finite fault model constructed from regional seismic data suggests that the rupture propagated unilaterally westward over a distance of approximately 50–60 km, with an average rupture velocity of 2.8 km/s (Calais et al., 2022). Two primary slip patches are evident along the fault. The first is located 0–30 km west of the epicenter, featuring ~1.9 m of slip dominated by reverse motion between depths of 0 and 12 km. The second patch lies ~40 km west of the epicenter and is confined to shallow depths (0–4 km), characterized by pure left-lateral strike-slip motion, with a peak slip of ~2.3 m. The source time function indicates a total rupture duration of approximately 20 seconds.

We gather PKIKP phase waveforms recorded by stations in Southeast Asia and Australia (Figures 5b and S19). The rupture process resolved by the PKIKP phase BP is illustrated in Figure 5a. The rupture propagated westward for approximately 57 km over a duration of 22 seconds, yielding an average rupture speed of 2.6 km/s (Figure 5b). The HF radiators resolved by the PKIKP BP are primarily distributed on the up-dip side of the major slip regions and are close to the fault traces (Figure 5a), further supporting the reliability of the BP results. For comparison, we also present the P phase BP results obtained by the Alaska array (Calais et al., 2022) in Figure 5. Remarkably, we observe consistency in the resolved rupture length and time between the two arrays. The rupture speed measured by the PKIKP BP (2.6 km/s) is consistent with that measured by the P phase BP (2.9 km/s, Calais et al., 2022). In contrast to the PKIKP BP image, the HF radiators resolved by the P BP do not align with the surface traces of the fault but are instead distributed along the down-dip edge of the major slip patch (Figure 5a). However, caution should be exercised when interpreting these distribution patterns, as the hosting fault is steeply north-dipping (60°, Calais et al., 2022; Douilly et al., 2022; Okuwaki & Fan, 2022), the along-dip dimension of the slip is only ~10 km, and the along-dip uncertainty levels are ~9.6 km for the P BP and ~9.4 km for the PKIKP BP, based on the test results in Section 3.2.

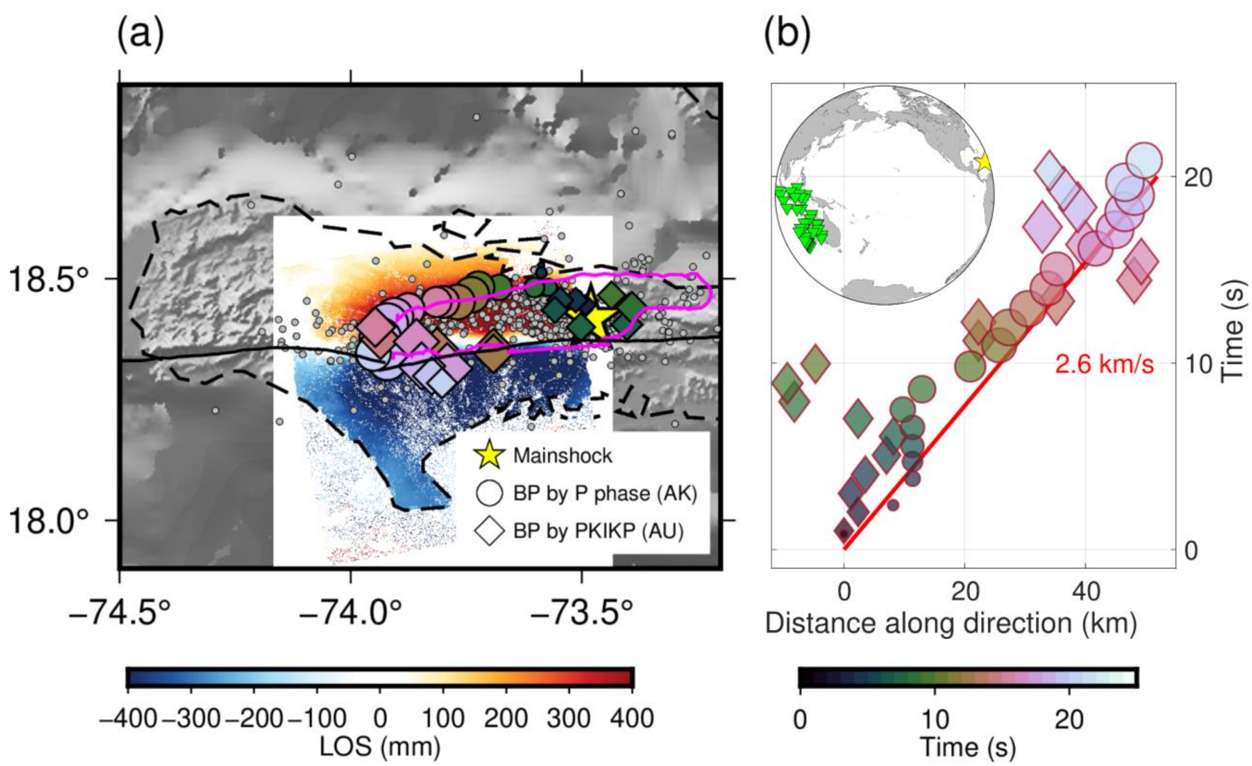

Figure 5. PKIKP phase BP results of the 2021 Mw 7.2 Haiti earthquake. (a) HF radiators evolution. The symbols are HF radiators color-coded by rupture time with their sizes proportional to the normalized BP power, with the circles denoting the P phase BP by Alaska (AK) array and the diamonds denoting the PKIKP phase BP by Australia and Southeast Asia (AU) array. The blue-to-red color denotes the ground displacement in Line of Sight (LOS) direction (Yin et al., 2022). Gray dots denote the aftershocks occurring between 14 August and 9 September 2021 (Calais et al., 2022). The magenta line encircles the major coseismic slip patch (>10% of the maximum slip; Raimbault et al., 2023). (b) The along-strike (N270°E) distance and time of HF radiators. The upper inset shows the stations used in PKIKP phase BP. The red line

and number show the linear regression of leading radiators and the rupture speed, based on the PKIKP BP by AU array.

4.3 The 2021 Mw 7.4 and Mw 8.1 Kermadec Earthquake Doublet

4.3.1 PKIKP BP Image of The 2021 Mw 7.4 Foreshock

On March 4, 2021, two closely occurring earthquakes took place near the Kermadec Islands. The first event, referred to as the foreshock, had a magnitude of Mw 7.4 and occurred at 17:41 UTC. The second event, known as the mainshock, had a magnitude of Mw 8.1 and occurred at 19:28 UTC. Both earthquakes are classified as reverse-slip events and took place in the Tonga-Kermadec subduction zone (Figures 6-7), which extends in a north-northeast direction from the North Island of New Zealand through Tonga to Samoa. Ye et al. (2025) constructed fault slip models for the earthquake doublet by integrating seismic, geodetic, and tsunami data. Their results indicate that the substantial coseismic slip during the Mw 8.1 mainshock occurred along the mantle–slab interface at depths of 20–55 km, with the major slip patch located to the north and north-northwest of the hypocenter, reaching a peak slip of 6 m. The Mw 7.4 foreshock nucleated near the down-dip edge of this region and propagated northeastward, with a peak slip of 2.5 m. Zeng et al. (2025) performed P-phase BP of the mainshock and found that the high-frequency sources were located at ~20 km depth along the up-dip edge of the major slip patch, coinciding with the intersection of the slab and forearc Moho, north of the hypocenter.

In our analysis, we utilize seismograms recorded at three arrays for performing BPs and making comparisons. Specifically, we use the PKIKP phase recorded at the Europe array, as well as the P phase recorded at the China array, and the P phase recorded at the Australia and Southeast (SE) Asia array (Text S3 in Supporting Information S1). To ensure consistency, all seismograms are filtered within the frequency range of 0.25 to 1 Hz. The hypocenter locations provided by USGS are adopted for our analysis (the foreshock: 29.68°S, 177.84°W, depth 43 km; the mainshock: 29.723°S, 177.279°W, depth 28.9 km). Figures 6a-c illustrate the spatio-temporal progression of HF radiators during the Mw 7.4 foreshock. In the same figures, we have plotted the slip model inverted by USGS for reference. Based on the evolution of HF radiators, we can divide the rupture process into two distinct stages. In stage 1, which spans the first 16 seconds, the rupture initiates with an up-dip propagation. It follows a linear path towards the northeast and terminates at the fault patch with the largest slip. This linear segment has a length of approximately 25 km, and the average propagation speed is estimated to be 1.6 km/s from the BP results of the Australia array (Figure 6e). It is noteworthy that all three arrays display similar rupture paths during stage 1. Moving to stage 2, some discrepancies emerge in the BP images obtained from the three arrays. In the BPs derived from the Europe array and the Australia-Asia array, the rupture initially appears to propagate back towards the hypocenter, and then it follows a circular path towards the east. Eventually, the HF rupture reaches a secondary slip area indicated by the slip model. On the other hand, in the BP images obtained from the China array, the rupture also follows a circular path during stage 2, but the direction is towards the north and northeast. The observed inconsistencies in stage 2 could be attributed to the array-dependent rupture pattern, which is often observed in complex rupture scenarios (e.g., Meng et al., 2011; Zhang et al., 2017). These variations may arise from factors such as directivity effects, interference between direct and depth phases, and the geometrical properties of isochrones (Bernard & Madariaga, 1984; Spudich & Frazer, 1984). Another possibility is that coda waves start to dominate the high-frequency signals, and the spatial locations of the HF radiators during stage 2 could be significantly distorted by the presence of coda waves.

4.3.2 PKIKP BP Image of The 2021 Mw 8.1 Mainshock

As shown in Figure 7, the HF radiators during the Mw 8.1 mainshock are observed to propagate towards the major slip patch identified in the USGS slip model. During the initial 30 seconds, the HF radiators imaged by all three arrays exhibit linear propagation. However, there are slight differences in their directions. The HF radiators obtained from the Australia array indicate a north-northwest rupture, while those obtained from the Europe and China arrays indicate a west-northwest direction. This discrepancy in rupture direction could be artifacts caused by the spatial biases inherent to the respective arrays' relative locations. To illustrate this, we apply the P BP (Figure S26a, c in Supporting Information S1) and the PKIKP BP (Figure S26b in Supporting Information S1) to several M5 earthquakes, utilizing the same travel time corrections as those adopted for the mainshock BP. The results highlight that the Australia array shows the least spatial error in the imaged rupture process. In contrast, the China and Europe arrays exhibit larger location errors as the rupture propagates farther from the epicenter. Overall, our BP results show general agreement with the USGS model, as the HF radiators coincide with the major slip asperities (Figure 7a-c).

4.3.3 Array-dependent Effect in BPs for Curved Ruptures

As presented in Section 4.3.1, the BP results for the Mw 7.4 foreshock exhibit discrepancies when analyzed using arrays from Australia, China, and Europe. This array-dependent effect has been noted in past subduction zone and bilateral strike-slip events (e.g., Meng et al., 2011; Xu et al., 2023). In addition to the spatial bias discussed in Section 4.3.2, another contributing factor to these discrepancies is the inherent complexity of rupture processes. In some subduction zone earthquakes, the rupture fronts are curved and expand widely in space (black curves in Figure 8). If the fault plane is shallow-dipping, such curved rupture fronts can yield different BP results when observed by arrays with different azimuths. To illustrate the array-dependent effect more clearly, we conduct two synthetic tests. In the first test, we use the rupture model of the Mw 7.4 foreshock from the USGS finite fault inversion as the input model. This rupture includes up to 3 m of slip on the 32.0° dipping fault plane and curved rupture fronts, as indicated by the slip initiation time contours shown in Figure 8. The fault is discretized into 0.01° by 0.01° grids. We apply the Yoffe analytic function with a 5 s rise time as the slip-rate function. Synthetic waveforms are calculated as the sum of slip-rate contributions from each subfault, convolved with EGFs. We synthesize teleseismic P waveforms recorded by arrays in Australia and China, and PKIKP waveforms at the Europe array. The synthetic BP results from these three arrays are displayed in Figure 8. While all three BP images highlight HF radiators with strong beam power at or near the major slip patch, the locations of these radiators differ. The Australia array's BP resolves the northwest aspect of the major slip patch, whereas the China and Europe arrays emphasize the central patch. Additionally, the radiators resolved by the China array extend further northeast than those observed by the other two arrays.

In the second test, we configure three point sources (Figure S27 in Supporting Information S1): source 1 ruptures at 0 s, while sources 2 and 3 rupture simultaneously at 10 s. All sources have a 5-s rise time. Source 1 is positioned at the hypocenter of the Mw 7.4 foreshock, source 2 is situated 22.2 km north of source 1, and source 3 is located 22.9 km east-northeast of source 1. During this test, all three arrays accurately image source 1. The Australia array successfully captures source 2 (Figure S27a in Supporting Information S1), while Europe and China arrays image source 3 (Figure S27b-c in Supporting Information S1).

These two synthetic tests clearly present the variations seen in BP images obtained from arrays at different azimuths. For each array, HF radiators are genuine, but they represent only parts of the curved rupture fronts. For earthquakes with complex rupture patterns, as often seen in nature, it is necessary to inspect BP results from multiple arrays for a more accurate interpretation of rupture kinematics.

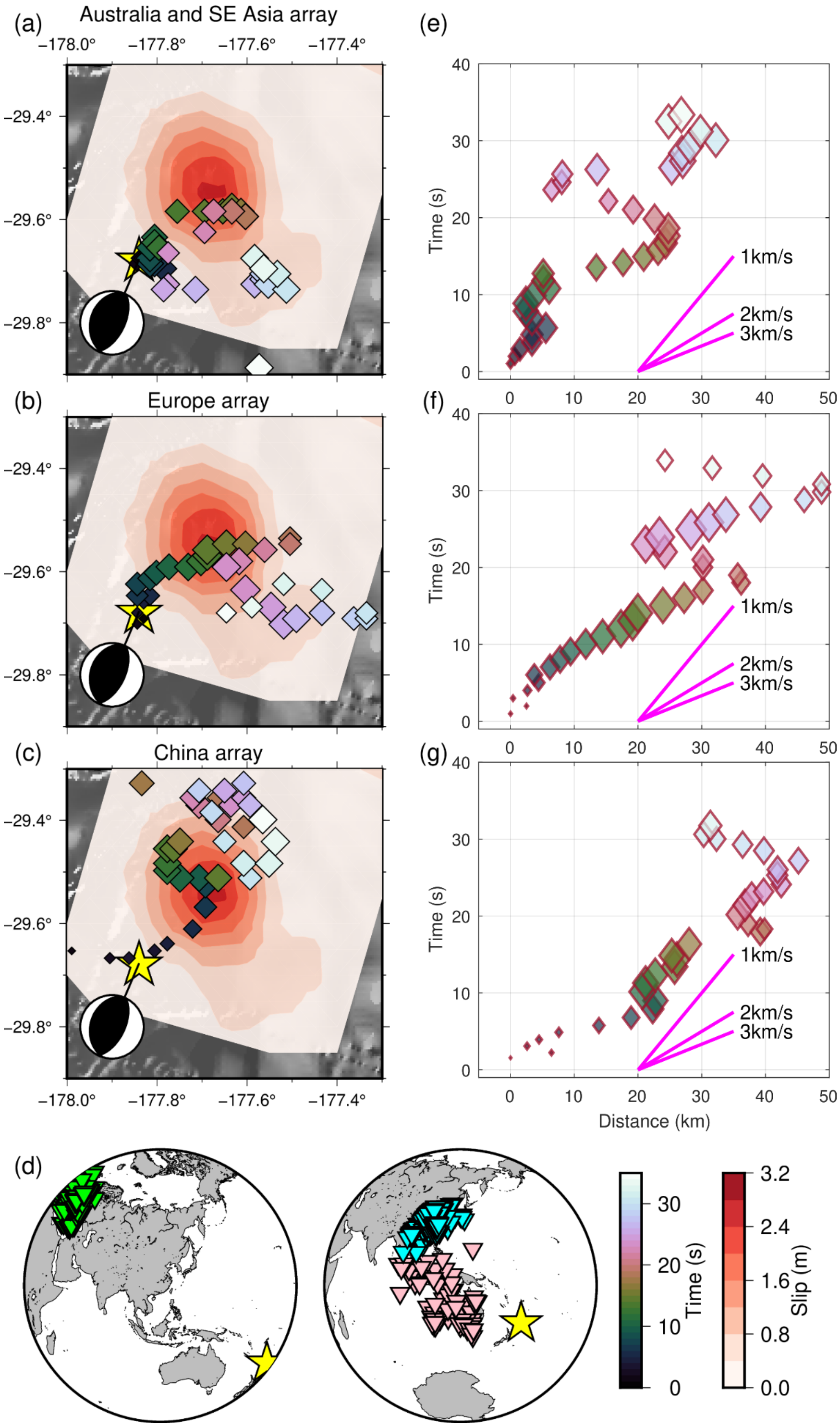

731

732 **Figure 6.** BPs of the 2021 Mw 7.4 foreshock. (a-c) HF radiators evolution resolved by the
733 Australia and southeast Asia array, Europe array, China array, respectively. The diamonds are
734 HF radiators color-coded by rupture time with their sizes proportional to the normalized BP
735 power. The contours denote the slip model from USGS. (d) Stations used for BPs. The green

triangles denote the Europe stations adopted in PKIKP phase BP, the pink triangles denote the SE Asia and Australia stations adopted in P phase BP, and the cyan triangles denote the China stations adopted in P phase BP. The yellow star denotes the epicenter. (e-g) The epicenter distance and time of HF radiators.

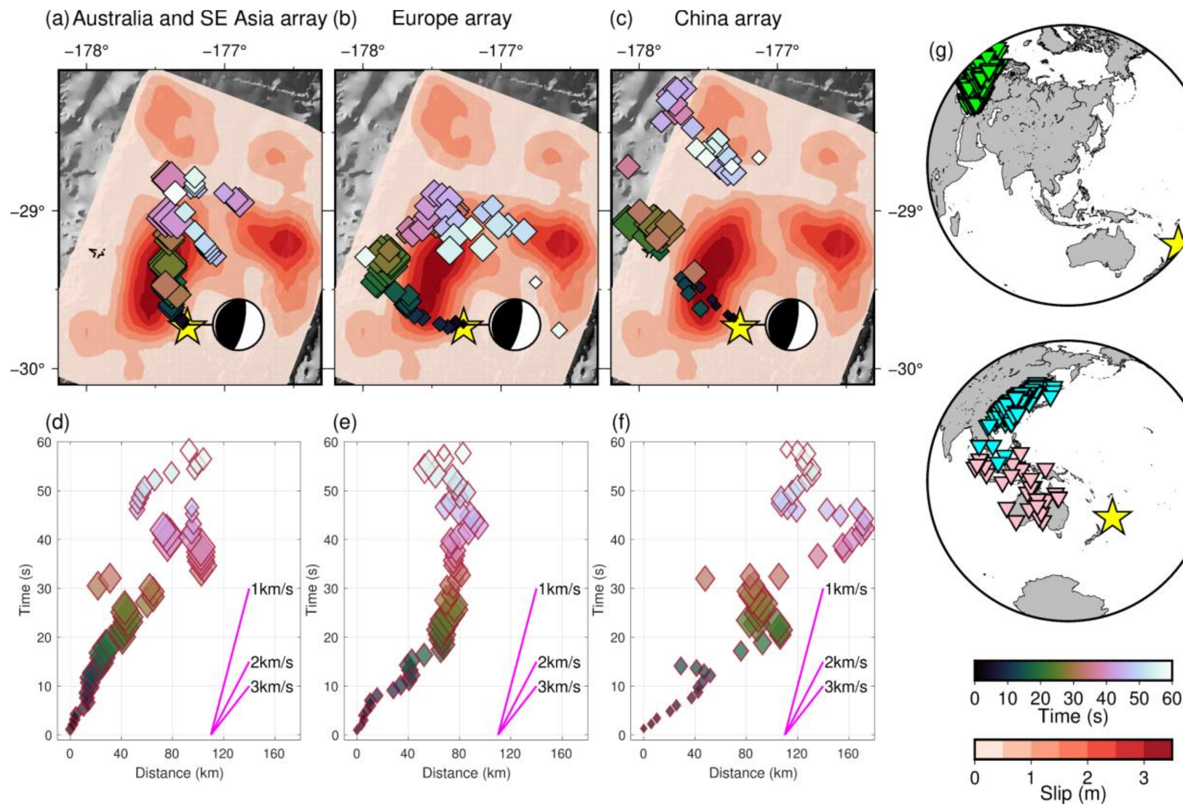

Figure 7. BPs of the 2021 Mw 8.1 mainshock. (a-c) HF radiators evolution resolved by the Australia and southeast Asia array, Europe array, China array, respectively. The diamonds are HF radiators color-coded by rupture time with their sizes proportional to the normalized BP power. The contours denote the slip model from USGS. (d-f) The epicenter distance and time of HF radiators. (g) Stations used for BPs. The green triangles denote the Europe stations adopted in PKIKP phase BP, the pink triangles denote the SE Asia and Australia stations adopted in P phase BP, and the cyan triangles denote the China stations adopted in P phase BP. The yellow star denotes the epicenter.

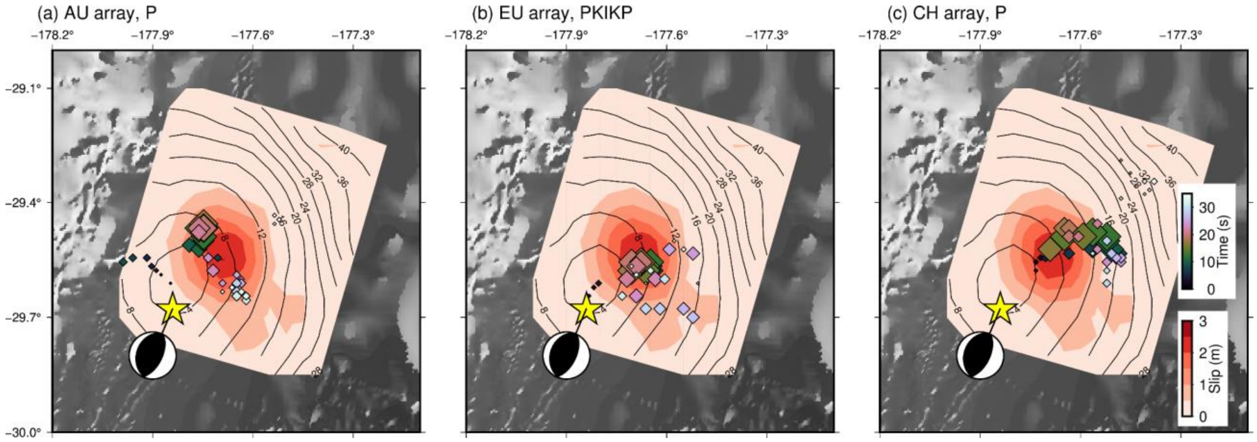

Figure 8. Synthetic BPs for the 2021 Mw 7.4 Kermadec earthquake. The reddish color background indicates the slip distribution resolved by USGS. The black time contours and numbers indicate the slip initiation time in the USGS slip model. (a) The synthetic BP imaged by the Australia (AU) array utilizing P phase. (b) The synthetic BP imaged by the Europe (EU) array utilizing PKIKP phase. (c) The synthetic BP imaged by the China (CH) array utilizing P phase. The diamonds' color indicates the time after the earthquake onset. The diamonds' size is proportional to the BP power.

5. Discussion

5.1 Assessment of Waveform and Wavefront Distortions in PKIKP Phase

Compared with the direct P phase recorded at teleseismic distances, which primarily propagates through the mantle, the PKIKP phase traverses both the core–mantle boundary (CMB) and the inner–outer core boundary. The CMB is known to exhibit strong heterogeneity (Haddon & Cleary, 1974; Garnero et al., 1988; Rost, 2013; Li et al., 2022b). To investigate potential waveform distortion (i.e., changes in waveform shape) and wavefront distortion (i.e., travel time variations) induced by heterogeneities, we analyze PKIKP and P waveforms of the 2021 Mw 8.1 Kermadec earthquake (Figures 9a and S28-S29). The P waveforms were recorded at teleseismic distances by the Chinese array (Figures 9a and S28), while the PKIKP waveforms were recorded at near-antipodal distances by the European array (Figures 9a and S29). We process and inspect the waveforms filtered in the 0.25–1 Hz band using the following steps:

(1) Initial alignment: All filtered waveforms are first aligned according to predicted P or PKIKP travel times from the 1D Earth model IASP91 (Kennett, 1991). Due to structural complexities in

the Earth's interior, this alignment remains approximate and introduces residual time errors (Figures S28a and S29a).

(2) Cross-correlation: For each trace, we extract a 10-second window following the P or PKIKP arrival. We compute cross-correlations (CCs) between each selected trace and all others, allowing a ±2 s time shift to maximize the CC. Traces with CCs below 0.7 would be removed.

(3) Reference trace selection and alignment: The trace that maintains the highest number of CCs above the threshold is selected as the reference trace (highlighted in red in Figures S28-S29). The aligned waveforms are shown in Figures S28b and S29b.

(4) Distortion evaluation: The CCs between all traces and the reference trace are presented in Figure 9a, while the corresponding time shifts are shown in Figure 9b.

For both P and PKIKP phases, most stations exhibit CC values greater than 0.7, and the corresponding time shifts are generally within ±1 s (Figure 9). Notably, no significant differences are observed in the CC or time-shift distributions between two phases. These findings suggest that, within the analyzed arrays, the degrees of waveform and wavefront distortion are comparable for both phases and are unlikely to degrade the quality of the PKIKP BP.

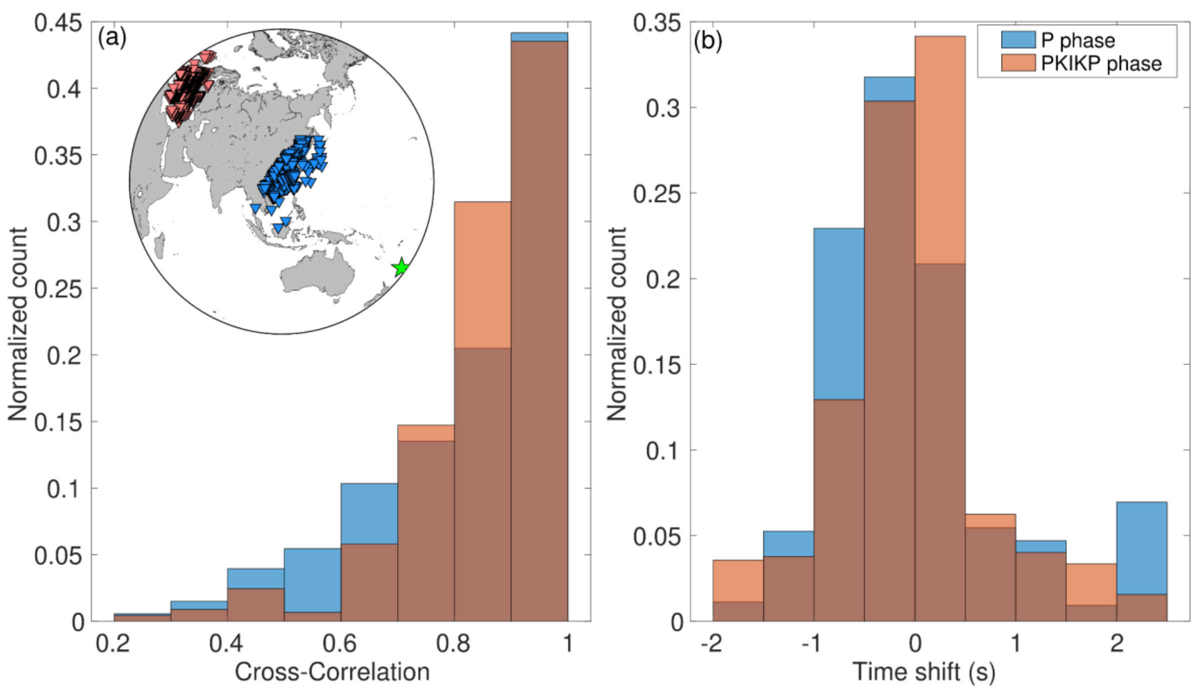

Figure 9. Distribution of cross-correlation coefficients (CCs) and time shifts. (a) Histogram of CCs relative to the reference trace. Blue bars represent the P phase; light red bars represent the PKIKP phase. The inset map shows the station distribution used for assessing waveform and wavefront distortions: blue triangles denote stations recording the P phase, and light red triangles denote stations recording the PKIKP phase. (b) Histogram of time shifts applied to each trace to maximize CC.

5.2 Advantages, Limitations, and Potential Improvements of PKIKP BP

Currently, most large and densely instrumented seismic networks with stable and publicly accessible data are located in the Northern Hemisphere, including the USArray, Alaska Array, European Array, Japanese Hi-net and F-net, and parts of the Chinese seismic array (Figure 10). In contrast, the Southern Hemisphere has limited coverage, with the Australian Array being the only network suitable for BP studies. To illustrate the spatial applicability of PKIKP BP, we plot global large earthquakes (Mw $\geq$ 7.0) that occurred between 2000 and 2022 in Figure 10. Earthquakes for which PKIKP BP is applicable are highlighted in red and purple. These events are primarily located in the southwest Pacific, along the western coast of South America, in the South Sandwich Islands of the South Atlantic, and in the southern Indian Ocean. In these regions, PKIKP BP can serve as a valuable reference when only one teleseismic array is available, or play a crucial role when no teleseismic array data is available. Furthermore, in some cases of bilateral earthquakes such as the aforementioned 2010 Mw 8.8 earthquake in Chile, the antipodal array exhibits a weaker array-dependent effect compared to the teleseismic array, resulting in a clearer image for the minor rupture branch. On the other hand, it also has several limitations. Under the same array configuration, PKIKP BP exhibits broader FWHM in its resolution kernels compared to P BP (Figure 1e), resulting in lower resolution. Additionally, when subjected to the same level of noise, PKIKP BP shows greater perturbation in the resolved source locations compared to P BP (Figures 1f and S7). Due to the longer travel paths of core phases through the Earth's interior, PKIKP BP results are also more susceptible to contamination from noise.

The 3D velocity heterogeneity of the Earth introduces uncertainties in BP results due to the path effect (Meng et al., 2016; Fan & Shearer, 2017). While the path effect has been investigated and corrected in some previous P phase BP studies (e.g., Meng et al., 2016; Fan & Shearer, 2017; Zeng et al., 2022; Zhang, 2019), it has not been explored in the context of PKIKP BP. Further research could focus on examining and mitigating the errors caused by the path effect in PKIKP BP to provide more accurate descriptions of earthquake processes. One potential solution to address the uncertainty is the application of Slowness-Enhanced Back-Projection (SEBP; Meng et al., 2016; Bao et al., 2019; Zhang, 2019). However, it should be noted that PKIKP phase has longer ray paths compared to direct P waves and traverses the highly heterogeneous inner core (Creager, 1997; Song, 2000; Vidale & Earle, 2000; Attanayake et al., 2018). Therefore, additional investigations are required to examine the travel time errors between realistic time and predictions based on 1-D velocity models. The first step in this process should involve checking if the spatial variation pattern of the travel time error is linear within the source region, which is a fundamental assumption of SEBP (Zhang, 2019; Zeng et al., 2022). Moreover, it is important to consider the complexities associated with the rotation processes of the outer and inner core, as their rotation rates and directions differ from other parts of the Earth (Song & Richards, 1996; Xu & Song, 2003; Yang & Song, 2023). Seismic phases traveling through the core from the same hypocenter to the same stations may experience changes in the ray path and travel time in a matter of decades or even shorter time scales (Vidale et al., 2022; Xu & Song, 2003; Yang & Song, 2023). Therefore, special caution is necessary when applying SEBP to the PKIKP phase. Foreshocks and aftershocks used to derive the slowness correction terms (Meng et al., 2016; Zhang, 2019) should be temporally close to the mainshock to avoid significant changes in the ray path and travel time. In addition, some multi-array approaches have been proposed to combine BP results from multiple arrays to image the 3D rupture paths (Xie et al., 2022) and reduce the inherent spatial bias (Vera et al., 2024). The application of PKIKP BP in these methods warrants further exploration.

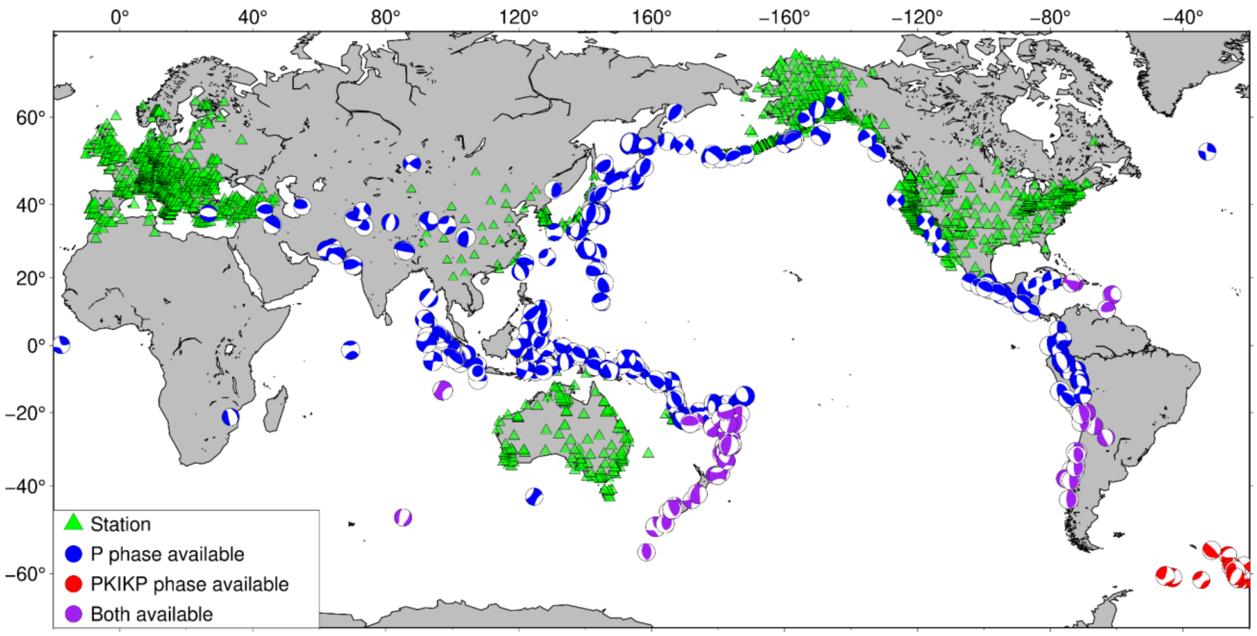

Figure 10. Focal mechanisms of all large (Mw>=7.0) earthquakes between 2000 and 2022, and large aperture arrays (green triangles). The focal mechanisms are color-coded by available arrays for teleseismic and PKIKP BP. Blue: only teleseismic P phase is available for BP. Red: only the PKIKP phase is available for BP. Purple: both teleseismic P and PKIKP phases are available for BP.

6. Conclusion

In this study, we back-project the PKIKP phase seismograms utilizing MUSIC algorithm to track the evolution of HF radiators during large earthquakes. To systematically evaluate the resolutions and uncertainties of PKIKP BP, we inspect ARF and BP images derived from theoretical seismograms, and conduct noise bootstrap tests. Our results indicate that the effective epicentral distance range for PKIKP BP is between 150° and 180°. Additional tests confirm that the influence of trailing PKPab and PKPbc phases is minimal. We then perform synthetic tests using unilateral rupture models, where we accurately recover the input rupture locations, lengths, and speeds. To further examine PKIKP BP's performance on natural large earthquakes, we apply our method to four events: the 2010 Mw 8.8 Chile earthquake, the 2021 Mw 7.2 Haiti earthquake, and the 2021 Kermadec Islands earthquake doublet. We inspect waveform coherence and compare our results with published studies, finding good agreement between PKIKP BP and previously reported teleseismic P BP images, surface fault traces, and finite-fault slip models. In comparison to teleseismic P BP, the PKIKP BP demonstrates improved performance in imaging some bilateral ruptures. This is observed in the BP analysis for the 2010 Mw 8.8 Chile earthquake and is further validated through a synthetic test. By analyzing waveform coherence and travel-time residuals in P and PKIKP seismograms of the 2021 Mw 8.1 Kermadec earthquake, we find that PKIKP exhibits similarly minor waveform and wavefront distortions as direct P. We finally discuss the advantages and limitations of our method, as well as potential future work. Given that many earthquake-prone regions in the southern hemisphere are located near the antipodes of large aperture arrays installed in the northern continents (e.g., USArray, Europe array, Alaska array), PKIKP BP have the potential to be a powerful tool for imaging the source process of earthquakes in these regions.

Acknowledgement

We thank Chen Ji for the fruitful discussion. We thank Eric Kiser and Mauro Palo for sharing the BP results of the Chile earthquake. We thank Bryan Raimbault and Romain Jolivet for sharing the slip model of the 2021 Haiti earthquake. The authors appreciate the insightful comments from anonymous reviewers, associate editors, and editor, which have greatly improved the manuscript. R. C is supported by the Natural Science Foundation of China (42325401). L.X and L.M are supported by the NSF grant (EAR-2506181). Figures were produced using Generic Mapping Tools (GMT, Wessel & Smith, 1998) and MATLAB. The Python software package ObSpy was used for data requests. The authors declare that they have no conflicts of interest.

Open Research:

Data Availability Statement

All seismic data are downloaded through the IRIS Wilber 3 system, ORFEUS, and the Data Management Center of China National Seismic Network, including the following seismic networks: (1) the AU (Australian National Seismograph Network Data Collection, Canberra, 2011); (2) the CZ (Czech Regional Seismic Network, Czech, 1973); (3) the EI (Dublin Institute for Advanced Studies, 1993); (4) the FR (RESIF, 1995); (5) the G (IPGP and EOST, 1982); (6) the GE (GEOFON Data Centre, 1993);(7) the GR (Federal Institute for Geosciences and Natural Resources, 1976); (8) the GU (University of Genoa, 1967); (9) the II (Scripps Institution of

Oceanography, 1986); (10) the IU (GSN; Albuquerque, 1988); (11) the IV (INGV Seismological Data Centre, 2006); (12) the MN (MedNet Project Partner Institutions, 1990); (13) the ND (Centre IRD de Noumea, Nouvelle-Caledonie, 2010); (14) the NL (KNMI, 1993); (15) the OE (ZAMG, 1987); (16) the OX (OGS, 2016); (17) the S1 (ANU, Australia, 2011); (18) the TA (Transportable Array; IRIS, 2003); (19) the TH (Institut fuer Geowissen-schaften, Friedrich-Schiller-Universitaet Jena, 2009); (20) the US (USNSN, Albuquerque, 1990). The MATLAB code of MUSIC BP is available at Xu and Meng (2024). Codes for PKIKP BP are available at Xu (2024).

References

Albuquerque Seismological Laboratory (ASL)/USGS. (1988). Global Seismograph Network (GSN - IRIS/USGS) [Dataset]. International Federation of Digital Seismograph Networks. https://doi.org/10.7914/SN/IU

Albuquerque Seismological Laboratory (ASL)/USGS. (1990). United States National Seismic Network [Dataset]. International Federation of Digital Seismograph Networks. https://doi.org/10.7914/SN/US

Australian National University (ANU, Australia). (2011). Australian Seismometers in Schools [Dataset]. International Federation of Digital Seismograph Networks. https://doi.org/10.7914/SN/S1

Attanayake, J., Thomas, C., Cormier, V. F., Miller, M. S., & Koper, K. D. (2018). Irregular transition layer beneath the Earth's inner core boundary from observations of antipodal PKIKP and PKIIKP waves. Geochemistry, Geophysics, Geosystems, 19, 3607– 3622. https://doi.org/10.1029/2018GC007562

Bao, H., Ampuero, J.-P., Meng, L., Fielding, E. J., Liang, C., Milliner, C. W. D., Feng, T., & Huang, H. (2019). Early and persistent supershear rupture of the 2018 magnitude 7.5 Palu earthquake. Nature Geoscience, 12(3), 200–205. https://doi.org/10.1038/s41561-018-0297-z

Bao, H., Xu, L., Meng, L., Ampuero, J.-P., Gao, L., & Zhang, H. (2022). Global frequency of oceanic and continental supershear earthquakes. Nature Geoscience, 15, 942–949. https://doi.org/10.1038/s41561-022-01055-5

Beavan, J., Samsonov, S., Denys, P., Sutherland, R., Palmer, N., & Denham, M. (2010). Oblique slip on the Puysegur subduction interface in the 2009 July MW 7.8 Dusky Sound earthquake from GPS and InSAR observations: Implications for the tectonics of southwestern New Zealand. Geophysical Journal International, 183(3), 1265–1286. https://doi.org/10.1111/j.1365-246X.2010.04798.x

Bernard, P., & Madariaga, R. (1984). A new asymptotic method for the modeling of near-field accelerograms. Bulletin of the Seismological Society of America, *74*(2), 539–557. https://doi.org/10.1785/bssa0740020539

Bonnardot, M. A., Régnier, M., Ruellan, E., Christova, C., & Tric, E. (2007). Seismicity and state of stress within the overriding plate of the Tonga-Kermadec subduction zone. Tectonics, 26(5), 1–15. https://doi.org/10.1029/2006TC002044

Born, M. Wolf, E. (1999). Principles of Optics. Cambridge University Press. p. 461. ISBN 0-521-64222-1.

Burnley, P. C., Green, H. W., & Prior, D. J. (1991), Faulting associated with the olivine to spinel transformation in Mg2GeO4 and its implications for deep-focus earthquakes, Journal of Geophysical Research, 96(B1), 425– 443, https://doi.org/10.1029/90JB01937.

Calais, E., Symithe, S., Monfret, T., Delouis, B., Lomax, A., Courboulex, F., Ampuero, J. P., et al. (2022). Citizen seismology helps decipher the 2021 Haiti earthquake. Science, 376(6590), 283–287. https://doi.org/10.1126/science.abn1045

Centre IRD de Noumea, Nouvelle-Caledonie. (2010). New CaleDonia Broadband Seismic Network [Dataset]. International Federation of Digital Seismograph Networks. https://doi.org/10.7914/SN/ND

Charles University in Prague (Czech), Institute of Geonics, Institute of Geophysics, Academy of Sciences of the Czech Republic, Institute of Physics of the Earth Masaryk University (Czech), & Institute of Rock Structure and Mechanics. (1973). Czech Regional Seismic Network [Dataset]. International Federation of Digital Seismograph Networks. https://doi.org/10.7914/SN/CZ

Chen, Y., Meng, L., Zhang, A., & Wen, L. (2018). Source Complexity of the 2015 Mw 7.9 Bonin Earthquake. Geochemistry, Geophysics, Geosystems, 19, 2109-2120. https://doi.org/10.1029/2018GC007489

Creager, K. C. (1997). Inner core rotation rate from small-scale heterogeneity and time-varying travel times. Science 278, 1284–1288. https://doi.org/10.1126/science.278.5341.1284

Delouis, B., Nocquet, J. M., & Vallée, M. (2010). Slip distribution of the February 27, 2010 Mw= 8.8 Maule earthquake, central Chile, from static and high-rate GPS, InSAR, and broadband teleseismic data. Geophysical Research Letters, 37(17). https://doi.org/10.1029/2010GL043899

Douilly, R., Paul, S., Monfret, T., Deschamps, A., Ambrois, D., Symithe, S. J., ... & Chèze, J. (2023). Rupture segmentation of the 14 August 2021 M w 7.2 Nippes, Haiti, earthquake using aftershock relocation from a local seismic deployment. Bulletin of the Seismological Society of America, 113(1), 58-72. https://doi.org/10.1785/0120220128

Du, H. (2021). Estimating Rupture Front of Large Earthquakes Using a Novel Multi-Array Back-Projection Method. Frontiers in Earth Science, 9. https://doi.org/10.3389/feart.2021.680163

Dublin Institute for Advanced Studies. (1993). Irish National Seismic Network [Dataset]. International Federation of Digital Seismograph Networks. https://doi.org/10.7914/SN/EI

Fan, W. Y., & Shearer, P. M. (2017). Investigation of backprojection uncertainties with M6 earthquakes. Journal of Geophysical Research: Solid Earth, 122(10), 7966–7986. https://doi.org/10.1002/2017jb014495

Federal Institute for Geosciences Natural Resources. (1976). German Regional Seismic Network (GRSN) [Dataset]. Other/Seismic Network. https://doi.org/10.25928/mbx6-hr74

Feng, T., Meng, L., & Huang, H. (2020). Detecting offshore seismicity: Combining backprojection imaging and matched-filter detection. Journal of Geophysical Research: Solid Earth, 125, e2020JB019599. https://doi.org/10.1029/2020JB019599

Garcia, R., Chevrot, S. & Weber M. (2004), Nonlinear waveform and delay time analysis of triplicated core phases, Journal of Geophysical Research, 109, B01306. https://doi.org/10.1029/2003JB002429.

Garnero, E., Helmberger, D., & Engen, G. (1988). Lateral variations near the core-mantle boundary. Geophysical Research Letters, 15(6), 609-612. https://doi.org/10.1029/GL015i006p00609

GEOFON Data Centre. (1993). GEOFON seismic network. GFZ Data Services [Dataset]. Other/Seismic Network. https://doi.org/10.14470/TR560404

Goldstein, P., & Archuleta, R. J. (1991), Deterministic frequency-wavenumber methods and direct measurements of rupture propagation during earthquakes using a dense array: Theory and methods, Journal of Geophysical Research, 96(B4), 6173–6185, https://doi.org/10.1029/90JB02123.

Gomberg, J., A. Wech, K. Creager, K. Obara, and D. Agnew (2016), Reconsidering earthquake scaling, Geophys. Res. Lett., 43, 6243–6251. https://doi.org/10.1002/2016GL069967

Green, H. W., & Burnley, P. (1989). A new self-organizing mechanism for deep-focus earthquakes. Nature, 341, 733–737. https://doi.org/10.1038/341733a0

Green, H. W., & Houston, H. (1995). The Mechanics of Deep Earthquakes. Annual Review of Earth and Planetary Sciences, 23(1), 169–213. https://doi.org/10.1146/annurev.ea.23.050195.001125

Guilbert, J., J. Vergoz, E. Schissele, A. Roueff, and Y. Cansi (2005). Use of hydroacoustic and seismic arrays to observe rupture propagation and source extent of the Mw = 9.0 Sumatra earthquake, Geophysical Research Letter, 32, L15310, https://doi.org/10.1029/2005GL022966.

Haddon, R. A. W., & Cleary, J. R. (1974). Evidence for scattering of seismic PKP waves near the mantle-core boundary. Physics of the Earth and Planetary Interiors, 8(3), 211-234. https://doi.org/10.1016/0031-9201(74)90088-0

Hayes, G. P. (2017). The finite, kinematic rupture properties of great-sized earthquakes since 1990. Earth and Planetary Science Letters, 468(June 2016), 94–100. https://doi.org/10.1016/j.epsl.2017.04.003

Hayes, G. (2018). Slab2 - A Comprehensive Subduction Zone Geometry Model: U.S. Geological Survey data release, https://doi.org/10.5066/F7PV6JNV.

Huang, Y.-L., Hwang, R.-D., Jhuang, Y.-S., & Lin, C.-Y. (2017). Rupture features of the 2010 Mw 8.8 Chile earthquake extracted from surface waves. Earth, Planets and Space, 69(1), 41. https://doi.org/10.1186/s40623-017-0624-4

INGV Seismological Data Centre. (2006). Rete Sismica Nazionale (RSN) [Dataset]. Istituto Nazionale di Geofisica e Vulcanologia (INGV). https://doi.org/10.13127/SD/X0FXNH7QFY

Institut fuer Geowissenschaften, Friedrich-Schiller-Universitaet Jena. (2009). Thüringer Seismologisches Netz [Dataset]. International Federation of Digital Seismograph Networks. https://doi.org/10.7914/SN/TH

Institut de Physique du Globe de Paris (IPGP) and Ecole et Observatoire des Sciences de la Terre de Strasbourg (EOST). (1982). GEOSCOPE, French global network of broad band seismic stations [Dataset]. Institut de Physique du Globe de Paris (IPGP). https://doi.org/10.18715/GEOSCOPE.G

IRIS Transportable Array. (2003). USArray Transportable Array [Dataset]. International Federation of Digital Seismograph Networks. https://doi.org/10.7914/SN/TA

Ishii, M., Shearer, P. M., Houston, H., & Vidale, J. E. (2005). Extent, duration and speed of the 2004 Sumatra-Andaman earthquake imaged by the Hi-Net array. Nature, 435(7044), 933–936. https://doi.org/10.1038/nature03675

Istituto Nazionale di Oceanografia e di Geofisica Sperimentale—OGS (2016). North-East Italy Seismic Network [Dataset]. FDSN. https://doi.org/10.7914/SN/OX

Kawai, K., Takeuchi, N. & Geller, R.J. (2006). Complete synthetic seismograms up to 2 Hz for transversely isotropic spherically symmetric media. Geophysical Journal International, 164, 411–424, https://doi.org/10.1111/j.1365-246X.2005.02829.x.

Karato, S., Riedel, M., & Yuen, D. (2001), Rheological structure and deformation of subducted slabs in the mantle transition zone: Implications for mantle circulation and deep earthquakes, Physics of the Earth and Planetary Interiors, 127(1–4), 83–108, https://doi.org/10.1016/S0031-9201(01)00223-0.

Kehoe, H. L., Kiser, E. D., & Okubo, P. G. (2019). The rupture process of the 2018 Mw 6.9 Hawai‘i earthquake as imaged by a genetic algorithm-based back-projection technique. Geophysical Research Letters, 46, 2467– 2474. https://doi.org/10.1029/2018GL080397

Kelemen, P. B., & Hirth, G. (2007), A periodic shear-heating mechanism for intermediate-depth earthquakes in the mantle, Nature, 446(7137), 787–90, https://doi.org/10.1038/nature05717.

Kennett, B.L.N. (Compiler and Editor). 1991. “IASPEI 1991 Seismological Tables.” Bibliotech, Canberra, Australia, 167 pp. https://doi.org/10.1111/j.1365-3121.1991.tb00863.x.

Kirby, S. H. (1987), Localized polymorphic phase transformations in high-pressure faults and applications to the physical mechanism of deep earthquakes, Journal of Geophysical Research, 92(B13), 13789– 13800, https://doi.org/10.1029/JB092iB13p13789.

Kirby, S. H., Durham, W. B., & Stern, L. A. (1991). Mantle phase changes and deep-earthquake faulting in subducting lithosphere. Science (New York, N.Y.), 252(5003), 216–225. https://doi.org/10.1126/science.252.5003.216

Kiser, E., and M. Ishii (2011), The 2010 Mw 8.8 Chile earthquake: Triggering on multiple segments and frequency-dependent rupture behavior, Geophys. Res. Lett., 38, L07301, https://doi.org/10.1029/2011GL047140.

Kiser, E., & Ishii, M. (2012). Combining seismic arrays to image the high-frequency characteristics of large earthquakes. Geophysical Journal International, 188(3), 1117–1128. https://doi.org/10.1111/j.1365-246X.2011.05299.x

Kiser, E., & Ishii, M. (2017). Back-Projection Imaging of Earthquakes. Annual Review of Earth and Planetary Sciences, 45(1), 271–299. https://doi.org/10.1146/annurev-earth-063016-015801

KNMI. (1993). Netherlands seismic and acoustic network. Royal Netherlands Meteorological Institute (KNMI) [Dataset]. Other/Seismic Network. https://doi.org/10.21944/e970fd34-23b9-3411-b366-e4f72877d2c5

Koper, K., Hutko, A., Lay, T., & Sufri, O. (2012). Imaging short-period seismic radiation from the 27 February 2010 Chile (MW 8.8) earthquake by back-projection of P, PP, and PKIKP waves. Journal of Geophysical Research, 117, B02308+. https://doi.org/10.1029/2011JB008576

Krim, H., and M. Viberg (1996), Two decades of array signal processing research: The parametric approach, IEEE Signal Process Mag., 13(4), 67–94, https://doi.org/10.1109/79.526899.

Lay, T., C. J. Ammon, H. Kanamori, K. D. Koper, O. Sufri, and A. R. Hutko (2010), Teleseismic inversion for rupture process of the 27 February 2010 Chile (Mw 8.8) earthquake, Geophys. Res. Lett., 37, L13301, https://doi.org/10.1029/2010GL043379.

Lay, T., H. Kanamori, C. J. Ammon, K. D. Koper, A. R. Hutko, L. Ye, H. Yue, and T. M. Rushing (2012), Depth-varying rupture properties of subduction zone megathrust faults, J. Geophys. Res., 117, B04311, https://doi.org/10.1029/2011JB009133.

Li, B., Wu, B., Bao, H., Oglesby, D. D., Ghosh, A., Gabriel, A.-A., et al. (2022a). Rupture heterogeneity and directivity effects in back-projection analysis. Journal of Geophysical Research: Solid Earth, 127(3), e2021JB022663. https://doi.org/10.1029/2021JB022663

Li, Z., Leng, K., Jenkins, J., & Cottaar, S. (2022b). Kilometer-scale structure on the core–mantle boundary near Hawaii. Nature Communications, 13(1), 2787. https://doi.org/10.1038/s41467-022-30502-5

Lin, Y. N. N., Sladen, A., Ortega-Culaciati, F., Simons, M., Avouac, J. P., Fielding, E. J., ... & Socquet, A. (2013). Coseismic and postseismic slip associated with the 2010 Maule Earthquake, Chile: Characterizing the Arauco Peninsula barrier effect. Journal of Geophysical Research: Solid Earth, 118(6), 3142-3159. https://doi.org/10.1002/jgrb.50207.

Madariaga, R. (1983). High frequency radiation from dynamic earthquake fault models. Annales de Geophysique, 1(1), 17–23. http://inis.iaea.org/search/search.aspx?orig_q=RN:14783441

Mahesh, P., Kundu, B., Catherine, J. K., & Gahalaut, V. K. (2011). Anatomy of the 2009 Fiordland earthquake (Mw 7.8), South Island, New Zealand. Geoscience Frontiers, 2(1), 17–22. https://doi.org/10.1016/j.gsf.2010.12.002

Maurer, J., Dutta, R., Vernon, A., & Vajedian, S. (2022). Complex rupture and triggered aseismic creep during the 14 August 2021 Haiti earthquake from satellite geodesy. Geophysical Research Letters, 49, e2022GL098573. https://doi.org/10.1029/2022GL098573

MedNet Project Partner Institutions. (1990). Mediterranean Very Broadband Seismographic Network (MedNet) [Dataset]. Istituto Nazionale di Geofisica e Vulcanologia (INGV). https://doi.org/10.13127/SD/FBBBTDTD6Q

Meng, L., Ampuero, J.-P., & Bürgmann, R. (2014), The 2013 Okhotsk deep-focus earthquake: Rupture beyond the metastable olivine wedge and thermally controlled rise time near the edge of a slab, Geophysical Research Letter, 41, 3779– 3785, https://doi.org/10.1002/2014GL059968.

Meng, L., Inbal, A., & Ampuero, J.-P. (2011), A window into the complexity of the dynamic rupture of the 2011 Mw 9 Tohoku-Oki earthquake, Geophysical Research Letter, 38, L00G07, doi:10.1029/2011GL048118.

Meng, L., Ampuero, J.-P., Sladen, A., & Rendon, H. (2012a), High-resolution backprojection at regional distance: Application to the Haiti M7.0 earthquake and comparisons with finite source studies, Journal of Geophysical Research, 117, B04313, doi:10.1029/2011JB008702.

Meng, L., Ampuero, J.-P., Stock, J., Duputel, Z., Luo, Y., & Tsai, V. C. (2012b). Earthquake in a Maze: Compressional Rupture Branching During the 2012 Mw 8.6 Sumatra Earthquake. Science, 337(6095), 724–726. http://www.jstor.org/stable/23268866

Meng, L., Zhang, A., & Yagi, Y. (2016). Improving back projection imaging with a novel physics-based aftershock calibration approach: A case study of the 2015 Gorkha earthquake. Geophysical Research Letters, 43(2), 628–636. https://doi.org/10.1002/2015GL067034

Meng, L., Bao, H., Huang, H., Zhang, A., Bloore, A., & Liu, Z. (2018). Double pincer movement: Encircling rupture splitting during the 2015 Mw 8.3 Illapel earthquake. Earth and Planetary Science Letters. 495. 164-173. https://doi.org/10.1016/j.epsl.2018.04.057.

Moreno, M., Melnick, D., Rosenau, M., Baez, J., Klotz, J., Oncken, O., ... & Hase, H. (2012). Toward understanding tectonic control on the Mw 8.8 2010 Maule Chile earthquake. Earth and Planetary Science Letters, 321, 152-165. https://doi.org/10.1016/j.epsl.2012.01.006.

Okuwaki, R., & Fan, W. (2022). Oblique convergence causes both thrust and strike-slip ruptures during the 2021 M 7.2 Haiti earthquake. Geophysical Research Letters, 49(2), e2021GL096373. https://doi.org/10.1029/2021GL096373

Palo, M., Tilmann, F., Krüger, F., Ehlert, L., & Lange, D. (2014). High-frequency seismic radiation from Maule earthquake (Mw 8.8, 2010 February 27) inferred from high-resolution backprojection analysis. Geophysical Journal International, 199(2), 1058–1077. https://doi.org/10.1093/gji/ggu311

Parsons, T. (2005). A hypothesis for delayed dynamic earthquake triggering. Geophysical Research Letters, 32(4), 1–4. https://doi.org/10.1029/2004GL021811

Pollitz, F. F., Brooks, B., Tong, X., Bevis, M. G., Foster, J. H., Bürgmann, R., ... & Blanco, M. (2011). Coseismic slip distribution of the February 27, 2010 Mw 8.8 Maule, Chile earthquake. Geophysical Research Letters, 38(9). https://doi.org/10.1029/2011GL047065

Prieto, G. A., M. Florez, S. A. Barrett, G. C. Beroza, P. Pedraza, J. F. Blanco, & E. Poveda (2013), Seismic evidence for thermal runaway during intermediate-depth earthquake rupture, Geophysical Research Letter, 40, 6064–6068, https://doi.org/10.1002/2013GL058109.

Raimbault, B., Jolivet, R., Calais, E., Symithe, S., Fukushima, Y., & Dubernet, P. (2023). Rupture geometry and slip distribution of the Mw 7.2 Nippes earthquake, Haiti, from space geodetic data. Geochemistry, Geophysics, Geosystems, 24, e2022GC010752. https://doi.org/10.1029/2022GC010752

RESIF. (1995). RESIF-RLBP French Broad-band network, RESIF-RAP strong motion network and other seismic stations in metropolitan France [Dataset]. RESIF—Réseau Sismologique et Géodésique Français. https://doi.org/10.15778/resif.fr

Romano, F., Gusman, A. R., Power, W., Piatanesi, A., Volpe, M., Scala, A., & Lorito, S. (2021). Tsunami Source of the 2021 MW 8.1 Raoul Island Earthquake From DART and Tide-Gauge Data Inversion. Geophysical Research Letters, 48(17). https://doi.org/10.1029/2021GL094449

Rost, S. (2013). Core–mantle boundary landscapes. Nature Geoscience, 6(2), 89-90. https://doi.org/10.1038/ngeo1715

Rost, S., & Thomas, C. (2002). Array seismology: Methods and applications. Reviews of Geophysics, 40(3), 2-1-2–27. https://doi.org/10.1029/2000RG000100

Schmidt, R. O. (1986), Multiple emitter location and signal parameter-estimation, IEEE Trans. Antennas Propag., 34(3), 276–280, https://doi.org/10.1109/ TAP.1986.1143830.

Schubnel, A., Brunet, F., Hilairet, N., Gasc, J., Wang, Y., & Green, H. W. (2013). Deep-Focus Earthquake Analogs Recorded at High Pressure and Temperature in the Laboratory. Science, 341(6152), 1377–1380. https://doi.org/10.1126/science.1240206

Scripps Institution of Oceanography. (1986). Global Seismograph Network - IRIS/IDA [Dataset]. International Federation of Digital Seismograph Networks. https://doi.org/10.7914/SN/II

Shearer, P. (2019). Introduction to Seismology (3rd ed.). Cambridge: Cambridge University Press. https://doi.org/10.1017/9781316877111

Spudich, P., & Frazer, L. N. (1984), Use of ray theory to calculate high-frequency radiation from earthquake sources having spatially-variable rupture velocity and stress drop, Bulletin of the Seismological Society of America, 74(6), 2061–2082.

Song, X., & Richards, P. G. (1996). Seismological evidence for differential rotation of the Earth's inner core. Nature, 382(6588), 221-224. https://doi.org/10.1038/382221a0

Song, X. (2000). Joint inversion for inner core rotation, inner core anisotropy, and mantle heterogeneity. Journal of Geophysical Research: Solid Earth 105, 7931–7943 (2000). https://doi.org/10.1029/1999JB900436.

Takeuchi, N., Geller, R.J. & Cummins, P.R. (1996). Highly accurate P-SV complete synthetic seismograms using modified DSM operators. Geophysical Research Letters, 23, 1175–1178, https://doi.org/10.1029/96GL00973.

Tinti, E., Fukuyama, E., Piatanesi, A., & Cocco, M. (2005). A Kinematic Source-Time Function Compatible with Earthquake Dynamics. Bulletin of the Seismological Society of America, 95(4), 1211–1223. https://doi.org/10.1785/0120040177

Thomson, D. J. (1982), Spectrum estimation and harmonic-analysis, Proc. IEEE, 70(9), 1055–1096, https://doi.org/10.1109/PROC.1982.12433.

Tkalčić, H., Romanowicz, B. & Houy, N. (2002), Constraints on D″ structure using PKP(AB–DF), PKP(BC–DF) and PcP–P traveltime data from broad-band records. Geophysical Journal International, 149: 599-616. https://doi.org/10.1046/j.1365-246X.2002.01603.x

Tong, X., Sandwell, D., Luttrell, K., Brooks, B., Bevis, M., Shimada, M., ... & Caccamise, D. J. (2010). The 2010 Maule, Chile earthquake: Downdip rupture limit revealed by space geodesy. Geophysical Research Letters, 37(24). https://doi.org/10.1029/2010GL045805.

Tsuji, T., Ashi, J., & Ikeda, Y. (2014). Strike-slip motion of a mega-splay fault system in the Nankai oblique subduction zone. Earth, Planets and Space, 66(1), 1–14. https://doi.org/10.1186/1880-5981-66-120

University of Genoa. (1967). Regional Seismic Network of North Western Italy [Dataset]. International Federation of Digital Seismograph Networks. https://doi.org/10.7914/SN/GU

Vera, F., Tilmann, F., & Saul, J. (2024). A decade of short-period earthquake rupture histories from multi-array back-projection. Journal of Geophysical Research: Solid Earth, 129, e2023JB027260. https://doi.org/10.1029/2023JB027260

Vidale, J. E. & Earle, P. S. (2000). Fine-scale heterogeneity in the Earth's inner core. Nature 404, 273–275. https://doi.org/10.1038/35005059

Vidale, J. E., Wang, W., Pang, G., & Koper, K. D. ~D. (2022). Complex inner core motion from LASA, ILAR, and YKA recordings. AGU Fall Meeting Abstracts, 2022, DI32B-0006.

Vigny, C., Socquet, A., Peyrat, S., Ruegg, J. C., Métois, M., Madariaga, R., ... & Kendrick, E. (2011). The 2010 M w 8.8 Maule megathrust earthquake of central Chile, monitored by GPS. Science, 332(6036), 1417-1421. https://doi.org/10.1126/science.1204132.

Wessel, P., & Smith, W. H. F. (1998). New, improved version of generic mapping tools released. Eos, Transactions American Geophysical Union, 79(47), 579. https://doi.org/10.1029/98EO00426

Xie, Y., Meng, L., Zhou, T., Xu, L., Bao, H., & Chu, R. (2022). The 2021 Mw 7.3 East Cape earthquake: Triggered rupture in complex faulting revealed by multi-array back-projections. Geophysical Research Letters, 49, e2022GL099643. https://doi.org/10.1029/2022GL099643

Xu, L., Yunjun, Z., Ji, C., Meng, L., Fielding, E. J., Zinke, R., & Bao, H. (2023). Understanding the rupture kinematics and slip model of the 2021 Mw 7.4 Maduo earthquake: A bilateral event on bifurcating faults. Journal of Geophysical Research: Solid Earth,128, e2022JB025936. https://doi.org/10.1029/2022JB025936

Xu, L. (2024). Matlab codes of core phase back-projections [Software]. Zenodo. https://doi.org/10.5281/zenodo.13888077

Xu, L., & Meng, L. (2024). MUltiple SIgnal Classification (MUSIC) Back-Projection (BP) [Software]. Zenodo. https://doi.org/10.5281/zenodo.12706948

Xu, X., & Song, X. (2003). Evidence for inner core super-rotation from time-dependent differential PKP traveltimes observed at Beijing Seismic Network. Geophysical Journal International, 152(3), 509–514, https://doi.org/10.1046/j.1365-246X.2003.01852.x

Yang, Y., & Song, X. (2023). Multidecadal variation of the Earth’s inner-core rotation. Nature Geoscience, 16, 182–187. https://doi.org/10.1038/s41561-022-01112-z

Yao, H., Gerstoft, P., Shearer, P. M., & Mecklenbräuker, C. (2011), Compressive sensing of the Tohoku-Oki Mw 9.0 earthquake: Frequency-dependent rupture modes, Geophysical Research Letters, 38, L20310, https://doi.org/10.1029/2011GL049223.

Ye, L., Hu, Y., Xia, T., Lay, T., Sang, Y., Chen, X., ... & Gui, Z. (2025). The 2021 MW 8.1 Kermadec earthquake sequence: Great earthquake rupture along the mantle/slab contact. Journal of Geophysical Research: Solid Earth, 130(4), e2024JB030926. https://doi.org/10.1029/2024JB030926

Yin, J. and Denolle, M. A. (2019), Relating teleseismic backprojection images to earthquake kinematics, Geophysical Journal International, 217(2), 729–747, https://doi.org/10.1093/gji/ggz048

Yin, H. Z., Xu, X., Haase, J. S., Douilly, R., Sandwell, D. T., & de Lepinay, B. M. (2022). Surface Deformation Surrounding the 2021 Mw 7.2 Haiti Earthquake Illuminated by InSAR Observations, Bulletin of the Seismological Society of America. 113, 41–57, https://doi.org/10.1785/0120220109

Yoffe, E. H. (1951). LXXV. The moving griffith crack. The London, Edinburgh, and Dublin Philosophical Magazine and Journal of Science, 42(330), 739-750. https://doi.org/10.1080/14786445108561302

Yue, H., Lay, T., Rivera, L., An, C., Vigny, C., Tong, X., & Báez Soto, J. C. (2014), Localized fault slip to the trench in the 2010 Maule, Chile Mw = 8.8 earthquake from joint inversion of high-rate GPS, teleseismic body waves, InSAR, campaign GPS, and tsunami observations, Journal of Geophysical Research: Solid Earth, 119, 7786– 7804, https://doi.org/10.1002/2014JB011340.

ZAMG—Zentralanstalt für Meterologie und Geodynamik. (1987). Austrian Seismic Network [Dataset]. International Federation of Digital Seismograph Networks. https://doi.org/10.7914/SN/OE

Zeng, H., Wei, S., & Rosakis, A. (2022). A travel-time path calibration strategy for back-projection of large earthquakes and its application and validation through the segmented super-shear rupture imaging of the 2002 Mw 7.9 Denali earthquake. Journal of Geophysical Research: Solid Earth, 127, e2022JB024359. https://doi.org/10.1029/2022JB024359

Zeng, H., Wei, S., & Yang, H. (2025). The 2021 Mw8. 1 Kermadec megathrust earthquake: An event rupturing the slab-mantle interface with up-dip high-frequency seismic energy radiation. Geophysical Research Letters, 52(4), e2024GL113015. https://doi.org/10.1029/2024GL113015

Zhan, Z. (2020). Mechanisms and Implications of Deep Earthquakes. Annual Review of Earth and Planetary Sciences, 48(1), 147–174. https://doi.org/10.1146/annurev-earth-053018-060314

Zhang, A. (2019). Theories and applications of enhanced earthquake back-projection imaging. eScholarship, University of California.

Zhang, H. (2018). Back-Projection Imaging the 2010 Mw 8.8 Chilean Earthquake. Imaging the Rupture Processes of Earthquakes Using the Relative Back-Projection Method: Theory and Applications, 77–84. https://doi.org/10.1007/978-3-662-55239-1_4.

Zhang, H., Koper, K. D., Pankow, K., & Ge, Z. (2017), Imaging the 2016 M w 7.8 Kaikoura, New Zealand, earthquake with teleseismic P waves: A cascading rupture across multiple faults, Geophysical Research Letter, 44, 4790–4798, https://doi.org/10.1002/2017GL073461.

Zhou, T., Meng, L., Zhang, A., & Ampuero, J.-P. (2022). Seismic waveform-coherence controlled by earthquake source dimensions. Journal of Geophysical Research: Solid Earth, 127, e2021JB023458. https://doi.org/10.1029/2021JB023458

Figure 1.

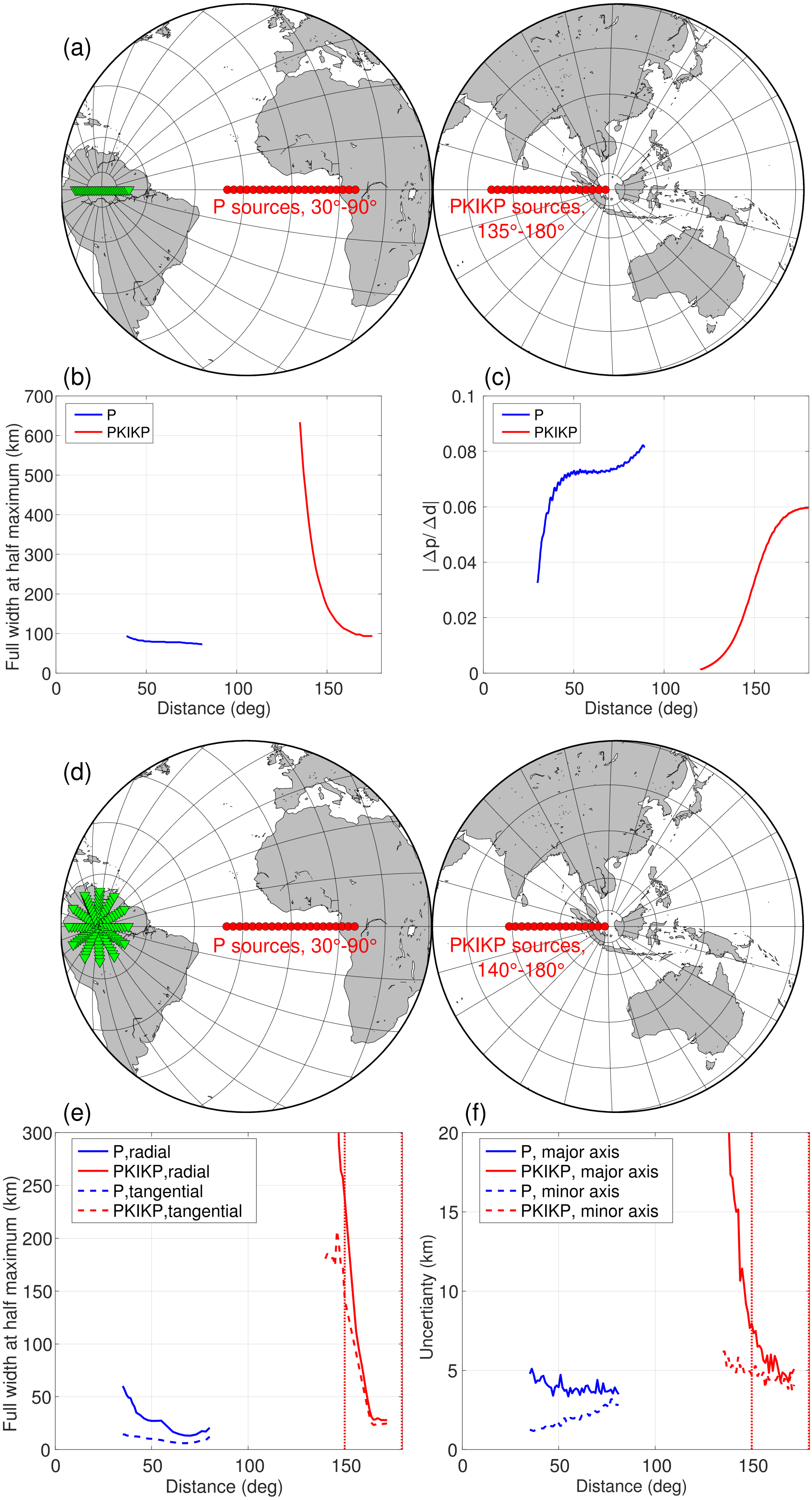

(a)
P sources, 30°-90°
PKIKP sources, 135°-180°
(b)
Full width at half maximum (km)
Distance (deg)
P
PKIKP
(c)
|Δp/Δd|
Distance (deg)
P
PKIKP
(d)
P sources, 30°-90°
PKIKP sources, 140°-180°
(e)
Full width at half maximum (km)
Distance (deg)
P,radial
PKIKP,radial
P,tangential
PKIKP,tangential
(f)
Uncertainty (km)
Distance (deg)
P, major axis
PKIKP, major axis
P, minor axis
PKIKP, minor axis

Figure 2.

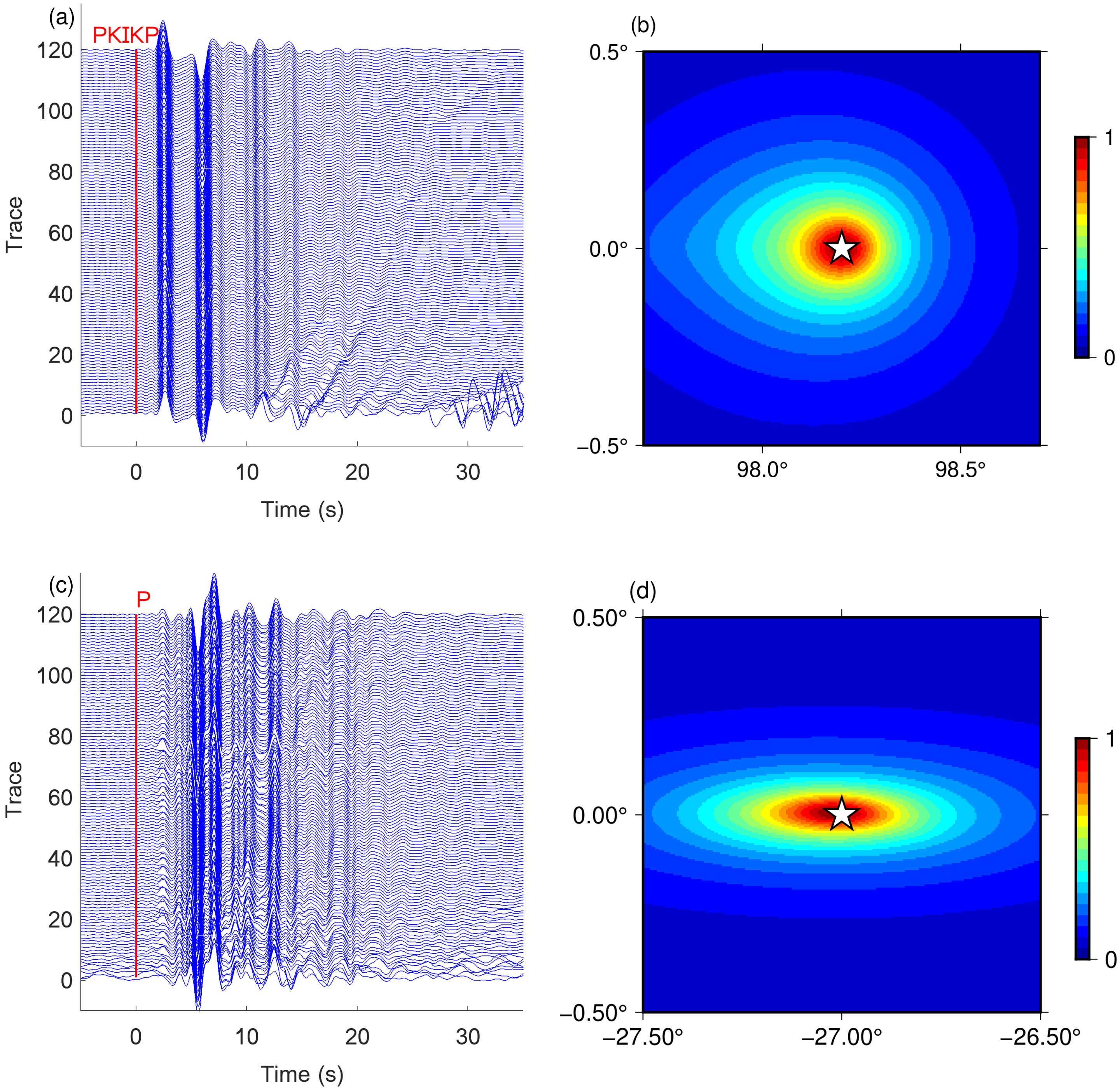
(a)
PKIKP
Trace
Time (s)
(b)
0.5°
0.0°
−0.5°
98.0°
98.5°
1
0
(c)
P
Trace
Time (s)
(d)
0.50°
0.00°
−0.50°
−27.50°
−27.00°
−26.50°
1
0

Figure 3.

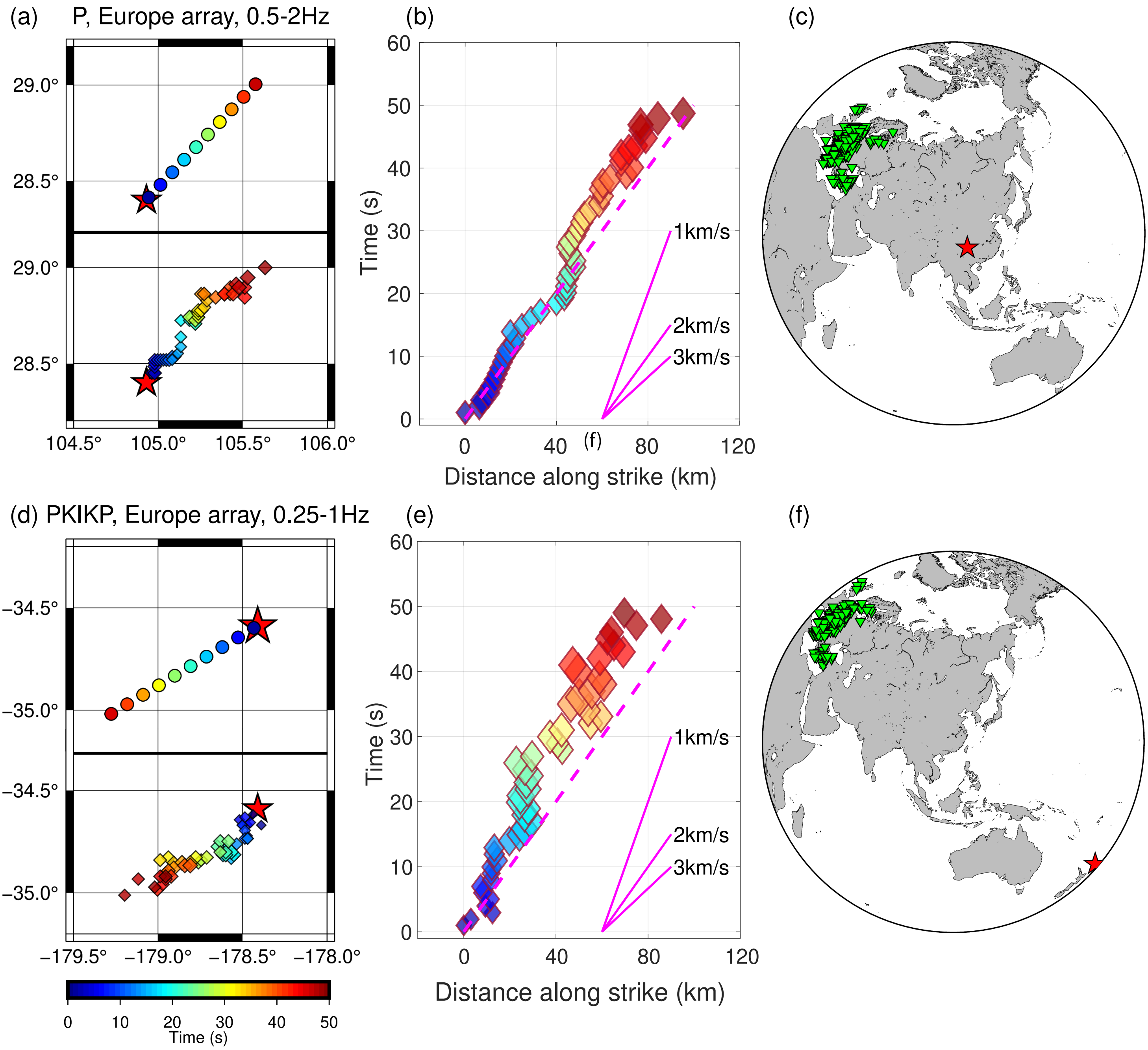

(a) P, Europe array, 0.5-2Hz
(b)
(c)
29.0°
28.5°
104.5°
105.0°
105.5°
106.0°
Time (s)
Distance along strike (km)
1km/s
2km/s
3km/s
(f)
(d) PKIKP, Europe array, 0.25-1Hz
(e)
(f)
–34.5°
–35.0°
–179.5°
–179.0°
–178.5°
–178.0°
Time (s)

Figure 4.

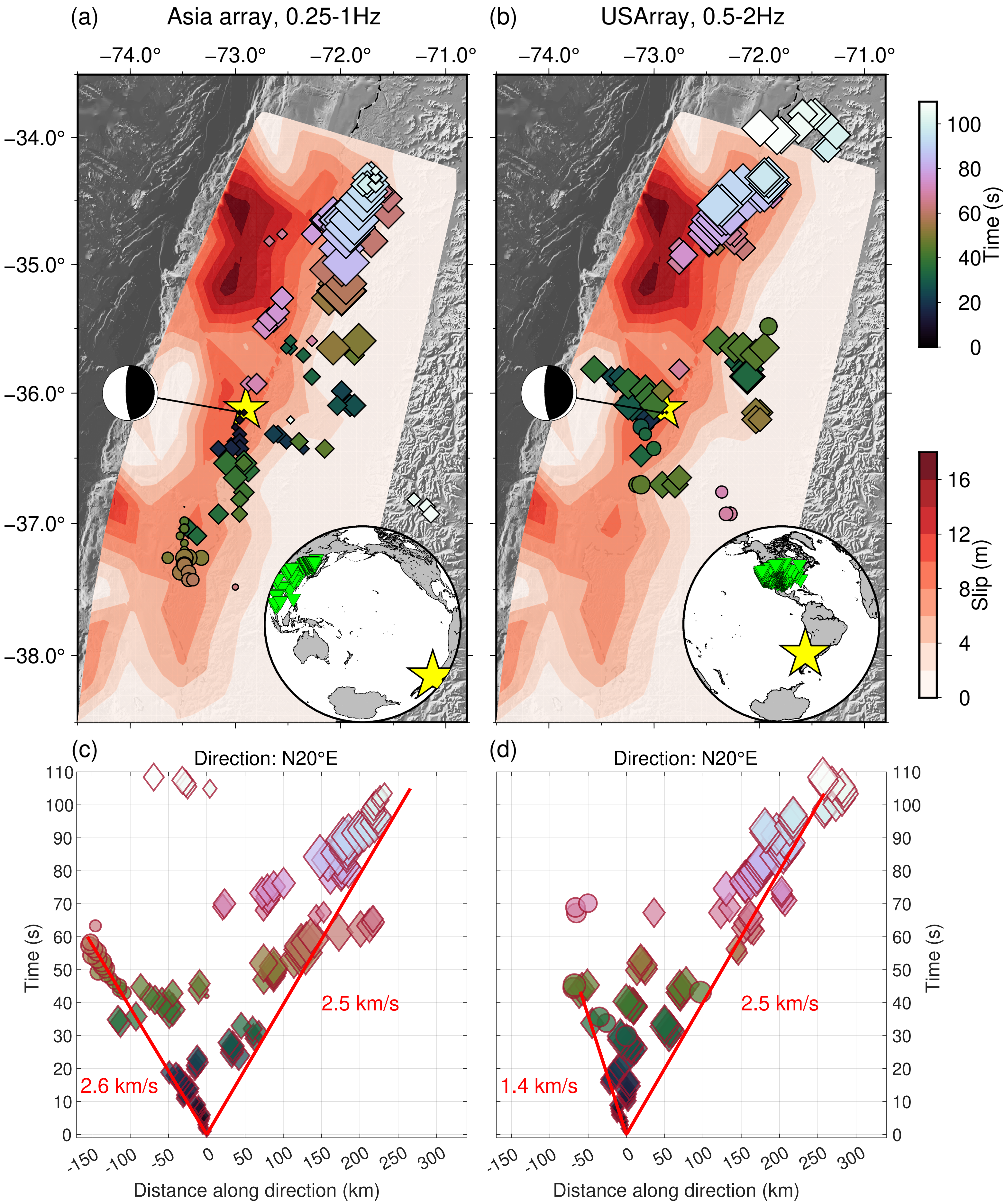

(a)
Asia array, 0.25-1Hz
(b)
USArray, 0.5-2Hz
−74.0°
−73.0°
−72.0°
−71.0°
−34.0°
−35.0°
−36.0°
−37.0°
−38.0°
Time (s)
0
20
40
60
80
100
Slip (m)
0
4
8
12
16
(c)
(d)
Direction: N20°E
2.6 km/s
2.5 km/s
1.4 km/s
Time (s)
Distance along direction (km)

Figure 5.

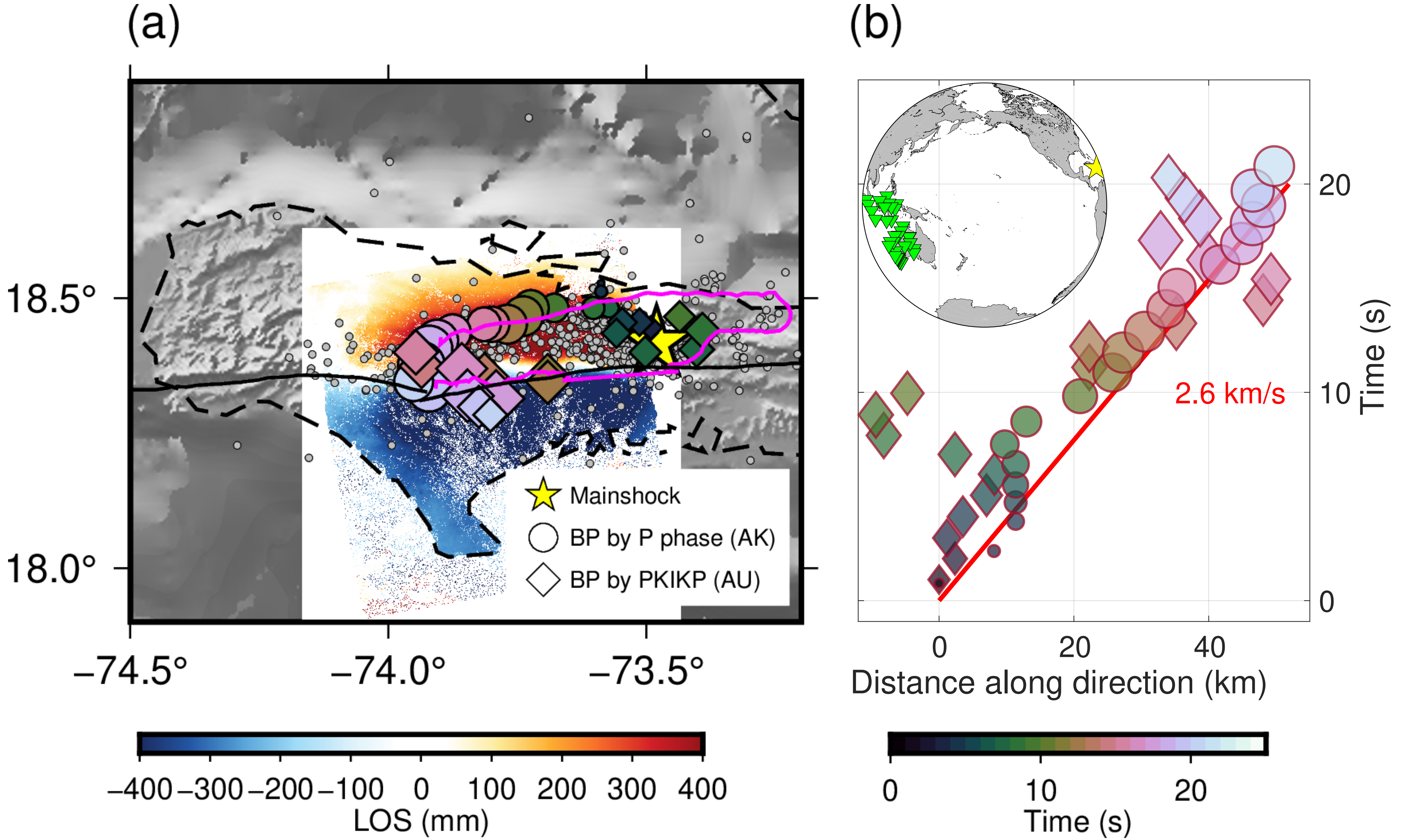

(a)
(b)
18.5°
18.0°
−74.5°
−74.0°
−73.5°
Mainshock
BP by P phase (AK)
BP by PKIKP (AU)
−400 −300 −200 −100 0 100 200 300 400
LOS (mm)
2.6 km/s
0
10
20
Time (s)
0
20
40
Distance along direction (km)
0 10 20
Time (s)

Figure 6.

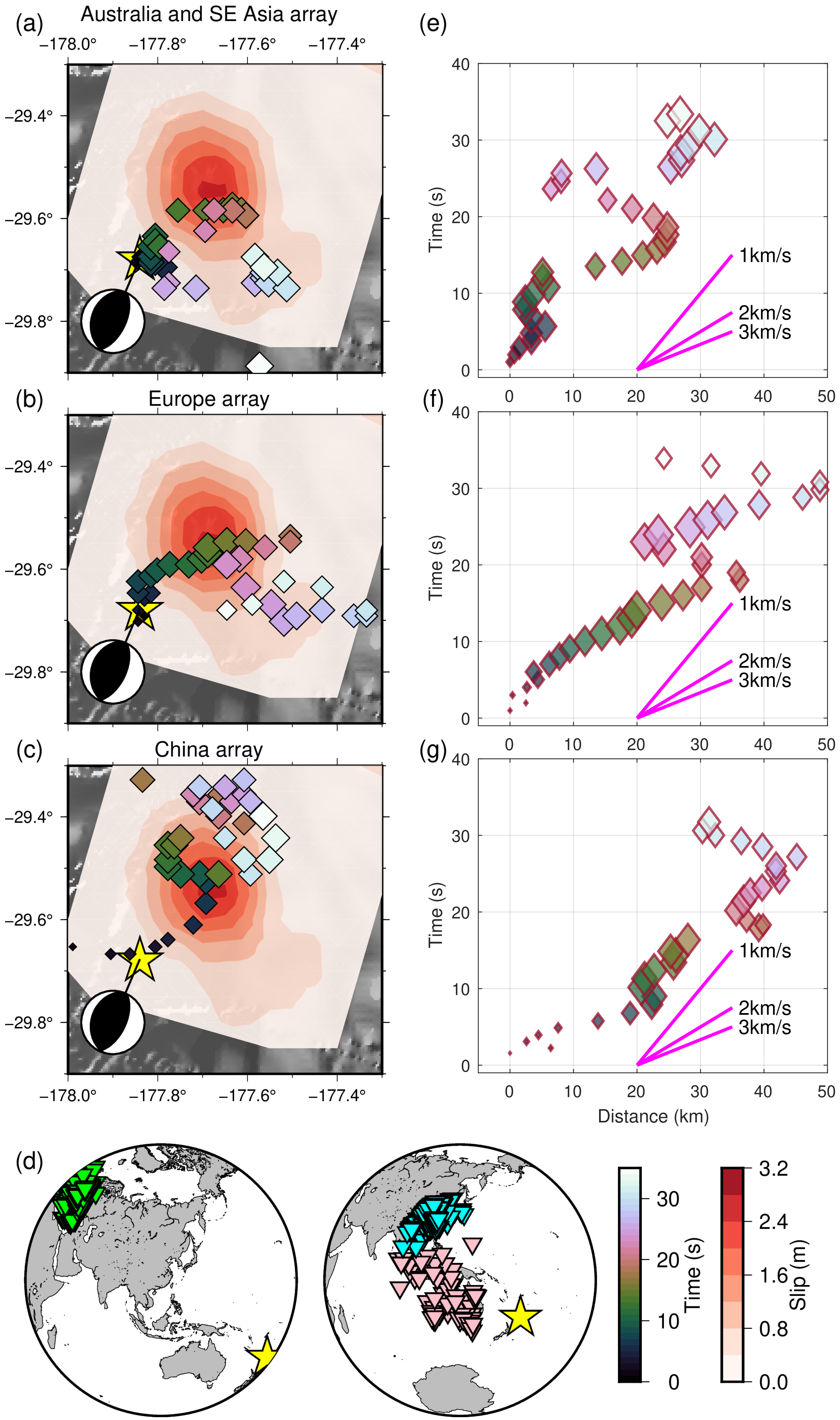

(a)
Australia and SE Asia array
–178.0°
–177.8°
–177.6°
–177.4°
–29.4°
–29.6°
–29.8°
(b)
Europe array
(c)
China array
(d)
(e)
(f)
(g)
Time (s)
Distance (km)
1km/s
2km/s
3km/s
Time (s)
Slip (m)
3.2
2.4
1.6
0.8
0.0

Figure 7.

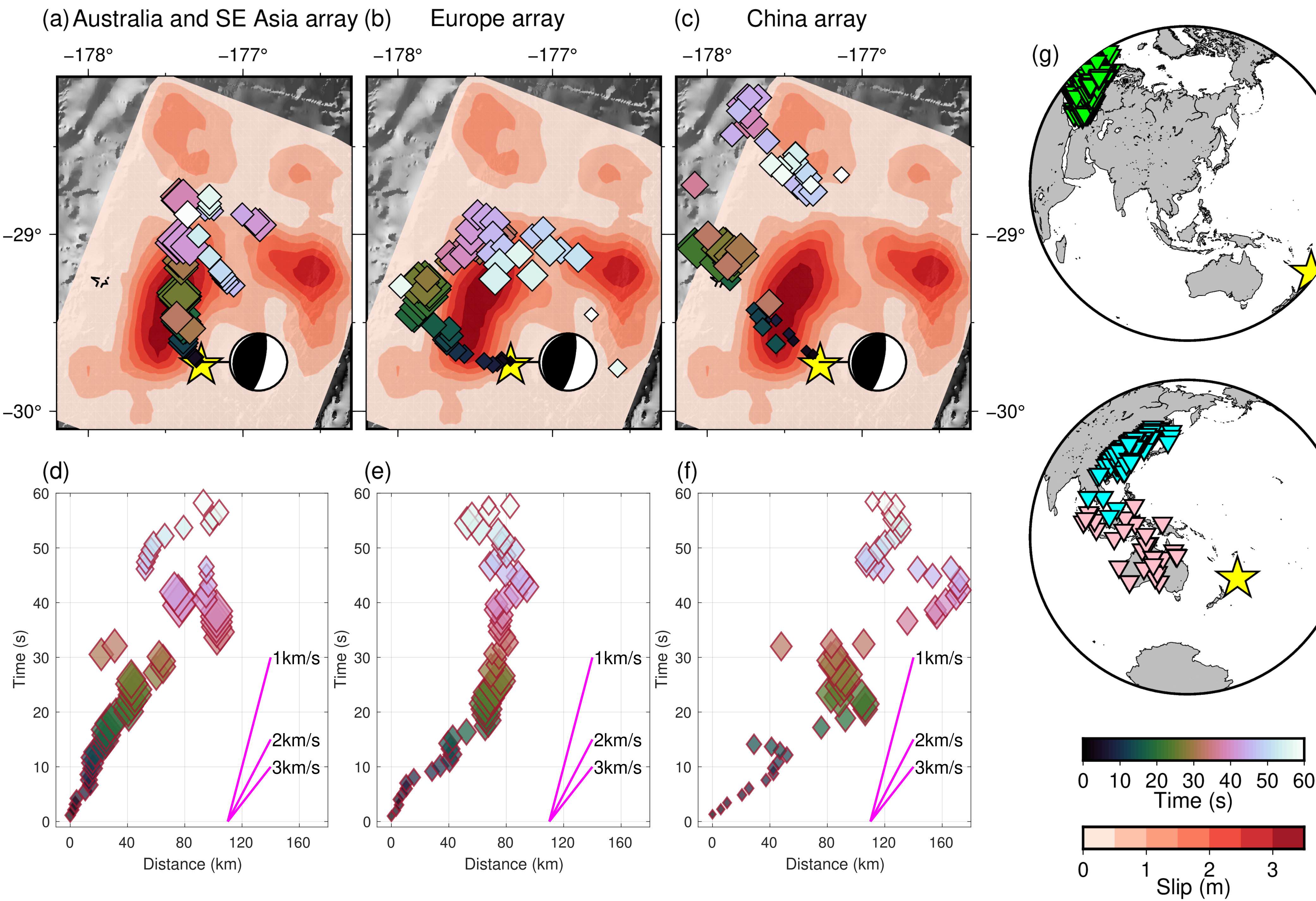

(a) Australia and SE Asia array
(b) Europe array
(c) China array
–178°
–177°
–29°
–30°
(g)
(d)
(e)
(f)
Time (s)
Distance (km)
1km/s
2km/s
3km/s
0
40
80
120
160
10
20
30
40
50
60
Time (s)
0 10 20 30 40 50 60
Slip (m)
0 1 2 3

Figure 8.

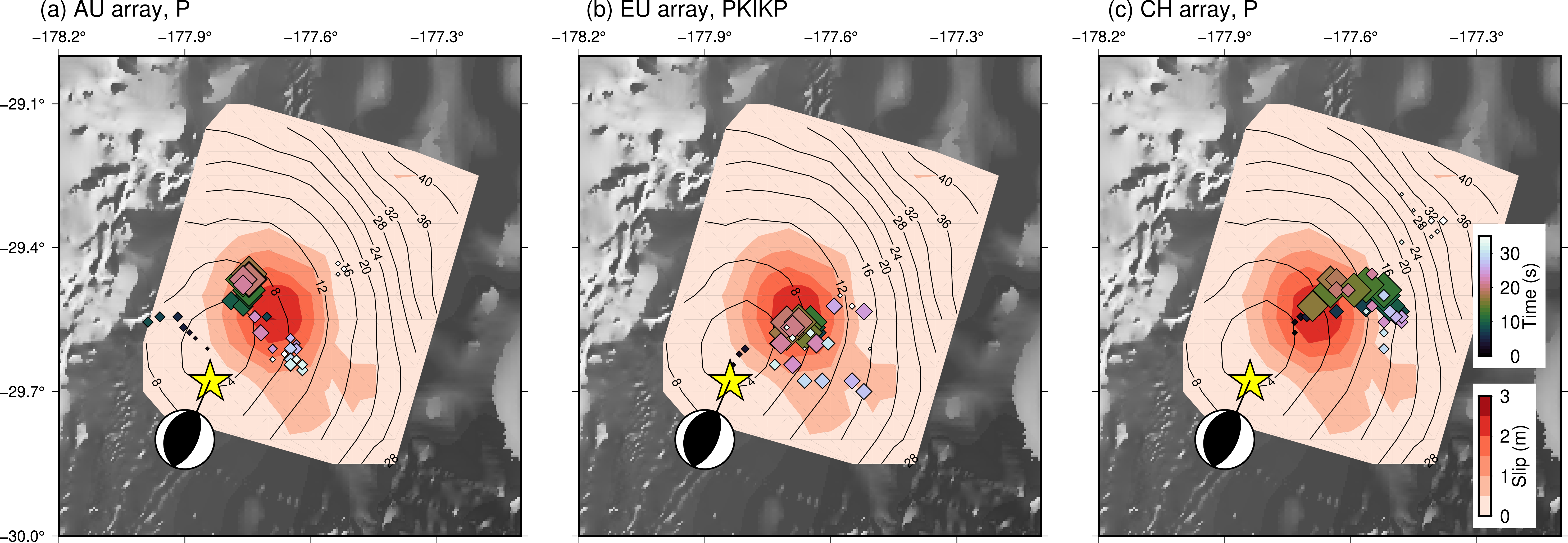

(a) AU array, P
(b) EU array, PKIKP
(c) CH array, P
–178.2°
–177.9°
–177.6°
–177.3°
–29.1°
–29.4°
–29.7°
–30.0°
Time (s)
0
10
20
30
Slip (m)
0
1
2
3

Figure 9.

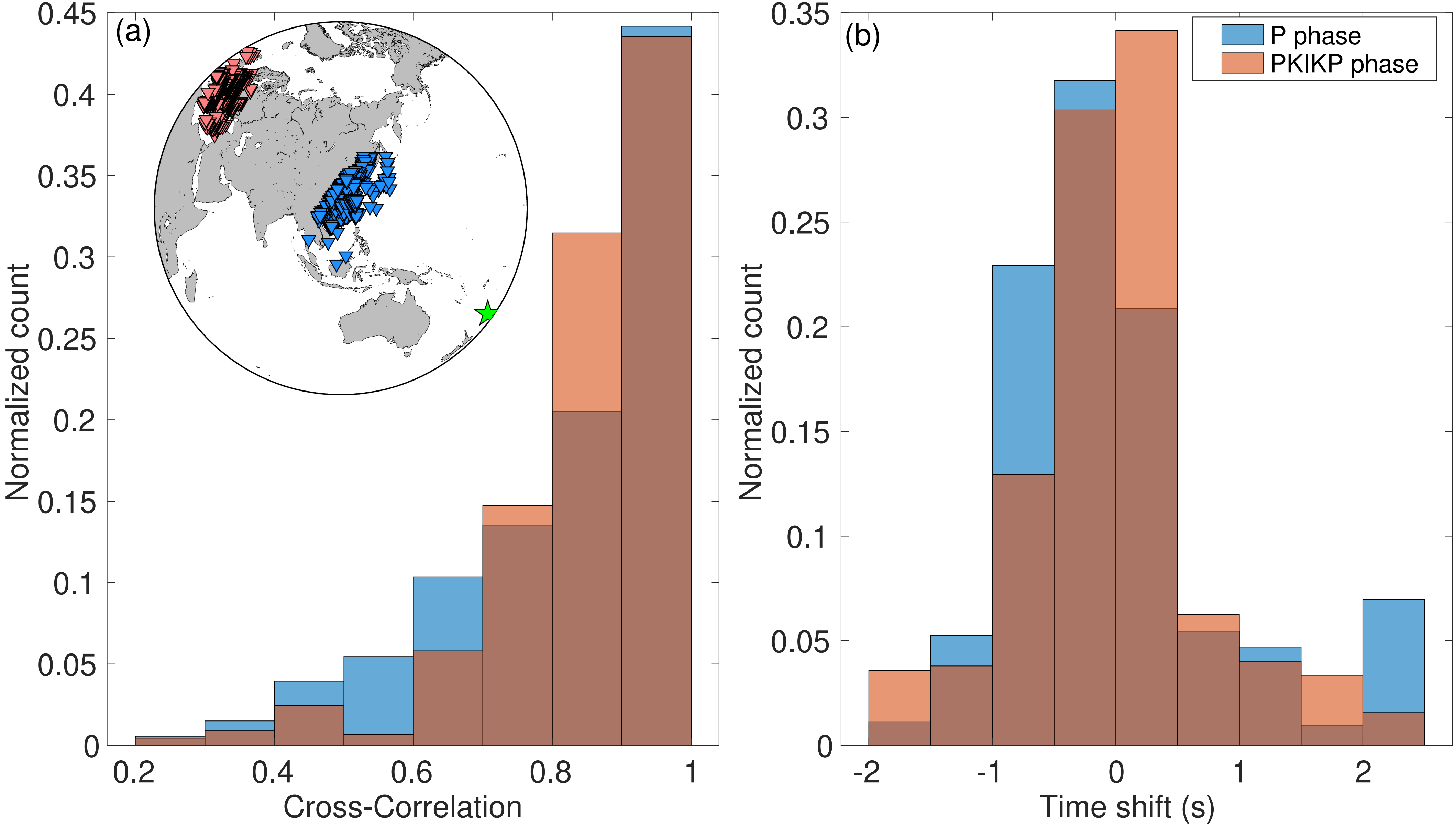
(a)
(b)
P phase
PKIKP phase
Normalized count
Cross-Correlation
Time shift (s)
0
0.05
0.1
0.15
0.2
0.25
0.3
0.35
0.4
0.45
0.2
0.4
0.6
0.8
1
-2
-1
0
1
2

Figure 10.

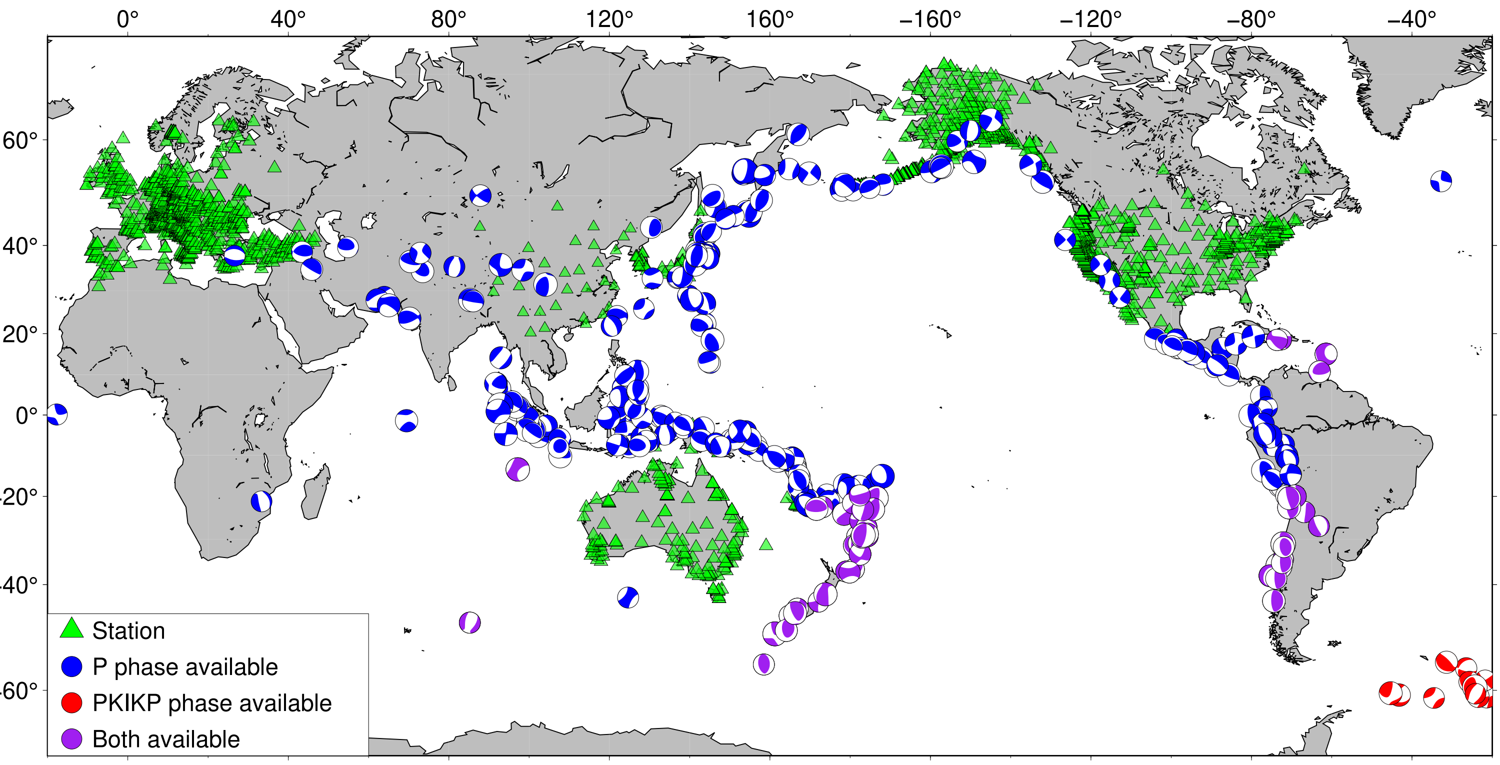

0°
40°
80°
120°
160°
−160°
−120°
−80°
−40°
60°
40°
20°
0°
−20°
−40°
−60°
Station
P phase available
PKIKP phase available
Both available